

Reply to Referee #1

General comments:

The impact of external thermal forcing induced atmospheric circulation changes on air quality is an important issue in atmospheric environment study. Focusing this scientific issue, this manuscript presented an interesting finding on two pathways of thermal forcing sources in the North Atlantic region (R1) and the western North Pacific region (R2) drive the interannual variations of autumnal haze pollution in the air pollution region of North China via the tele-connection analysis and AGCM simulation, which could improve our understanding and prediction on air quality change in China, Asia and the Northern Hemisphere. This manuscript falls within the scope of ACP. I suggest the minor revisions before it is published as follows:

Reply: Thank you for your positive comments. We have revised the manuscript based on your comments/suggestions. Below is our point-by-point reply to these comments/suggestions (italic is for original comments and non-italic is our replies).

Specific comments:

1)*Please add the discussions on the tele-connection pattern from the R1 region to North China in connection with North Atlantic Oscillation, and the R2 region in association with Western Pacific Warm Pool.*

Reply: Thanks for your comment. We have added two relevant references and corresponding discussions. Please see **Lines 220-223** and **Lines 254-255** in the revised manuscript for the discussions.

(Lines 220-223) “Intriguingly, from the surface projection of the above quasi-barotropic teleconnection pattern, we can discern a positive phase of North Atlantic Oscillation-like mode in connection with this pattern (Hurrell and Deser, 2009).”

(Lines 254-255) “...with its southern portion belonging to the Western Pacific Warm Pool (You et al., 2018).”

Reference:

Hurrell, J. W., and Deser, C.: North Atlantic climate variability: The role of the North Atlantic Oscillation, *J Marine Syst*, 78, 28-41, 10.1016/j.jmarsys.2008.11.026, 2009.

You, Y. C., Cheng, X. G., Zhao, T. L., Xu, X. D., Gong, S. L., Zhang, X. Y., Zheng, Y., Che, H. Z., Yu, C., Chang, J. C., Ma, G. X., and Wu, M.: Variations of haze pollution in China modulated by thermal forcing of the Western Pacific Warm Pool, *Atmosphere*, 9, 314, 10.3390/atmos9080314, 2018.

2) Please modify the lines 20-21: the joint impacts can greatly enhance the likelihood of a higher AHD_{BTH} . Observational and simulation evidence suggests that SST anomalies can affect the variation....

Reply: Thanks for your comment. The modification was done. Please see Lines 22-24 in the revised manuscript.

Lines 22-24: "...When the autumnal SST warming in R1 and R2 are both significant, the likelihood of a higher AHD_{BTH} is greatly enhanced. Observational and simulation evidence demonstrated how SST anomalies over R1 and R2 influence variation of AHD_{BTH} via two different pathways."

3) Lines 191 and 193, please add "surface air" before "temperature".

Reply: Thanks for your suggestion. We have added "surface air" before "temperature". Please see Line 205 in the revised manuscript.

Line 205: "...and surface air temperature (Fig. 4b), ..."

4) Please add the box outlines the research domain of the BTH region in Fig. 7.

Reply: Thanks for your constructive suggestion. We have added the blue dashed box outlining the research domain of the BTH region. Please see Fig. 7 in the revised manuscript.

Reply to Referee #2

General comments:

This paper provides a new possible signal source in the North Atlantic subtropical sector (R1) and the western North Pacific sector (R2) for autumnal haze days (AHD) in the Beijing-Tianjin-Hebei region (BTH region) via the tele-connection mode. The effect sequence of the warm phase of these two oceanic sources on the AHD in BTH is basically reasonable, leading to depressed planetary boundary layer and subsidence of the atmosphere. These changing meteorological conditions are the favorable background for the higher AHD in BTH. The methodology used in this paper is correct (i.e. Rossby wave train). The findings obtained by this paper may be useful to make the seasonal outlook of the air pollution condition in autumn.

Reply: Thank you for your positive comments. We have revised the manuscript based on your comments/suggestions. Below is our point-by-point reply to these comments/suggestions (italic is for original comments and non-italic is our replies).

Specified corrections:

(1) For the SST of the North Atlantic, why only the middle oceanic region is selected? The representative signal source of the AMO should be the triple-pole SST pattern, with high-latitude and the tropical poles being more important.

Reply: Thanks for your comment. The AMO is known as the SST in the North Atlantic varying on the basin scale and at period of around 65–80 years. Since our study concentrated on the interannual variability, the AMO is not relevant to our research target.

We chose subtropical North Atlantic region (22°–32°N, 90°–40°W) as the key SSTA region for the following two reasons. Firstly, the subtropical North Atlantic SSTA is the only region over North Atlantic that highly correlated with the AHD_{BTH} on interannual timescale. Although the regression SSTA pattern over North Atlantic looks like a tri-pole SST pattern (NAT SST pattern for short) which has profound impacts on Eurasian climate, the relationship between AHD_{BTH} and simultaneous NAT SST pattern is insignificant. The correlation coefficient between AHD_{BTH} and NAT SST triple-pole index (Deser and Michael, 1997) is only 0.17. Therefore, we chose the middle oceanic region of North Atlantic as the key region for AHD_{BTH} .

Secondly, the positive correlated SSTA over that region can induce positive rainfall anomaly (diabatic heating). Therefore, the SSTA should play an active role in local air-sea interaction and in turn influence the large-scale circulation through inducing teleconnection.

To sum up, we chose subtropical North Atlantic region (22°–32°N, 90°–40°W) as the key driving region from both statistical diagnosis and physical basis.

We have added this discussion in the revised manuscript (Lines 255-266).

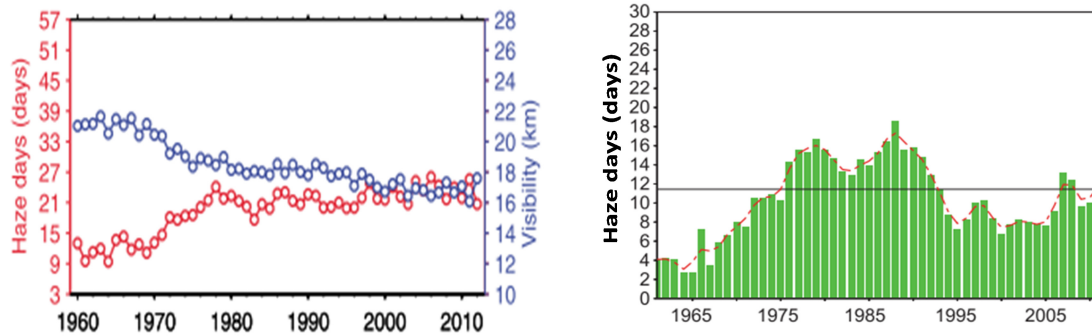
Reference:

Deser, C. and Michael S.T., 1997: Atmosphere-ocean interaction on weekly timescales in the North Atlantic and Pacific. *Journal of Climate*, 10(3): 393-408.

(2) From Figure 2, one can see the rapid increase of AHD in BTH. However, other studies have shown that the rapid increase in AHD started from the mid-ninety of 20 century or early in this century. Please compare the difference between them and explain why.

Reply: Thanks for your constructive comments. After checking many related literatures (e.g., **Figure 6b** in Fu and Dan, 2014), we found that the annual total haze days indeed showed the rapid increase in the BTH region since the early 21st century, but it is not materialized for the case of autumn season.

For the autumn season, from the previous studies, we found that the rapid increase in AHD over North China did not start from the mid-ninety of 20 century or early in this century (**R-Figure 1**). Our results are quite consistent with the previous studies.



R-Figure 1. Time series of AHD in North China. (left) Adapted from *Chen and Wang (2015)*. (right) Adapted from *Ding and Liu (2014)*. The red dashed line is 9-point smooth curve.

Reference:

Chen, H. P., and Wang, H. J.: Haze Days in North China and the associated atmospheric circulations based on daily visibility data from 1960 to 2012, *J Geophys Res Atmos*, 120, 5895-5909, 10.1002/2015JD023225, 2015.

Ding, Y. H., and Liu, Y. J.: Analysis of long-term variations of fog and haze in China in recent 50 years and their relations with atmospheric humidity, *Sci China Earth Sci*, 57, 36-46, 10.1007/s11430-013-4792-1, 2014.

Fu, C. B., and Dan, L.: Spatiotemporal characteristics of haze days under heavy pollution over central and eastern China during 1960–2010, *Climatic and Environmental Research (in Chinese)*, 19 (2), 219-226, 2014.

(3) For Figure 6, please indicate the significance level for the correlation coefficient.

Reply: Thanks for your suggestion. We have added the significance level for the correlation coefficient as suggested. Please see Figure 6 in the revised manuscript.

(4) The anticyclonic circulation over Northeast China-Okhotsk Sea at 850 hPa is a critical system. Please check if it only takes place in autumn (or/and winter)? Whether or not it already exists in summer?

Reply: Thanks for your good comment and suggestion. As you indicated, the 850-hPa anomalous anticyclonic circulation over Northeast China-Okhotsk Sea is indeed a critical system that having significant impacts upon the interannual variability of AHD_{BTH}. In addition to autumn season, this system also takes place in winter (e.g., **Figure 4b** in Yin et al., 2017; **Figure 3a** in Zhong et al., 2018), which greatly influences the interannual changes of wintertime haze pollution.

However, this anticyclonic circulation does not exist in the prior summer based on our correlation analysis (figures omitted). Therefore, we could infer that this

anticyclonic circulation anomaly over Northeast Asia is only occurred in the simultaneous autumn and winter.

Reference:

Yin, Z. C., Wang, H. J., and Chen, H. P.: Understanding severe winter haze events in the North China Plain in 2014: roles of climate anomalies, *AtmosChemPhys*, 17, 1641-1651, 10.5194/acp-17-1641-2017, 2017.

Zhong, W. G., Yin, Z. C., Wang, H. J., and: The Relationship between the Anticyclonic Anomalies in Northeast Asia and Severe Haze in the Beijing–Tianjin–Hebei Region, *AtmosChem Phys, Discuss.*, 10.5194/acp-2018-782, in review, 2018.

(5) From Figure 10(a), the descending motion seems to be out of BTH region. Please explain it.

Reply: Thanks for your comment. Except for a small portion of upward motion over the southern BTH region, most of the BTH region is indeed dominated by air subsidence from mid-to-upper troposphere (700-300 hPa in Figure 10a).

The significant descending motion is tied to strong ascending motion over south of the BTH region. Because the ascending motion is so strong, it makes the descending motion farther to the north. Nevertheless, this subsidence could enhance Northeast Asian anticyclonic anomaly.

(6) The warm R2 should be associated with the El Nino event. Therefore, according the EAP pattern, it could be “- + -“ meridional circulation pattern. Please attention to this point and further properly modify the position A in Figure 13.

Reply: Thanks for your insightful suggestion. The El Niño event related to EAP pattern (or PJ pattern) mainly appears in boreal summer. The present study focuses on the autumn season. We think Northeast Asian anticyclonic anomaly is not part of the EAP pattern, but rather a joint result of the mid-latitude Rossby wave train emanating from Atlantic to East Asia, and an anomalous local meridional circulation forced by western North Pacific SSTA.

Two pathways of how remote SST anomalies drive the interannual variability of autumnal haze days in the Beijing–Tianjin–Hebei region, China

Jing Wang¹, Zhiwei Zhu^{1*}, Li Qi¹, Qiaohua Zhao¹, Jinhai He¹, and Julian X. L. Wang²

¹Key Laboratory of Meteorological Disaster, Ministry of Education (KLME)/Joint International Research Laboratory of Climate and Environment Change (ILCEC)/Collaborative Innovation Center on Forecast and Evaluation of Meteorological Disasters (CIC-FEMD), Nanjing University of Information Science and Technology, Nanjing, China

²Air Resources Laboratory, National Oceanic and Atmospheric Administration, College Park, MD, USA

* Correspondence to: Zhiwei Zhu (zww@nuist.edu.cn)

Abstract. Analogous to the circumstances in wintertime, the increasing severity of autumnal haze pollution over the Beijing–Tianjin–Hebei (BTH) region may also lead to impairment of the socioeconomic development and human health in this region. Despite manmade aerosol emissions, the interannual variability of autumnal (September–October–November) haze days (AHD) in the BTH region (AHD_{BTH}) is apparently tied to the global and regional meteorological anomalies. The present study suggests that an above-normal AHD_{BTH} is closely associated with the simultaneous sea surface temperature (SST) warming in two regions [over the North Atlantic subtropical sector (R1) and over the western North Pacific sector (R2)]. ~~When the autumnal SST warming in R1 and R2 are both remarkably significant, the joint impacts can greatly enhance the likelihood of a higher AHD_{BTH} . Observational and simulation evidence suggests that SST anomalies can affect the variation in AHD_{BTH} via two different pathways.~~ When the autumnal SST warming in R1 and R2 are both significant, the likelihood of a higher AHD_{BTH} is greatly enhanced. Observational and simulation evidence demonstrated how remote SST anomalies over R1 and R2 influence variation of AHD_{BTH} via two different pathways. Firstly, SST warming in R1 can induce a downstream mid-latitude Rossby wave train, leading to a barotropic high-pressure and subsidence anomaly over the BTH region. Secondly, SST warming in R2 can also result in air subsidence over the BTH region through an anomalous local meridional cell. Through these two distinct pathways, localized meteorological circumstances conducive to a higher AHD_{BTH} (i.e., repressed planetary boundary layer, weak southerly airflow, and warm and moist conditions) can be established.

1 Introduction

Aerosol particles (APs) are ubiquitous in the ambient air. Through aerosol-induced thermal forcing, APs can exert profound impacts on regional and large-scale circulation (e.g., Chung et al., 2002; Lau and Kim, 2006; Lau et al., 2006; Liu et al., 2009; Li et al., 2016; Wu et al., 2016), as well as global warming (e.g., Charlson et al., 1992; Tett et al., 1999; Zhang et al., 2016). Notably, due to the property of light extinction related to high concentrations of APs, especially fine particulate matter [i.e., particulate matter (PM) with an aerodynamic diameter of 2.5 μm or less ($PM_{2.5}$)] (Guo et al., 2014; Wang et al., 2014; Li et al., 2017; Seo et al., 2017; Chen et al., 2018; Luan et al., 2018), severe haze weather with low visibility ~~and high concentrations of gas pollutants~~ can readily occur (Chen et al., 2012; Li et al., 2016; Ding et al., 2017; Seo et al., 2017; Chen et al., 2018).

In recent decades, observational evidence suggests that China has become one of the most severe AP-loading regions in the world (Tao et al., 2016; Li et al., 2016), arguably because of the country's nationwide rapid industrialization and urbanization (Xu et al., 2015; Zhang et al., 2016). High concentrations of APs can lead to the formation of severe haze weather via complicated interactions (Wang et al., 2014). Haze weather is not only harmful to the human respiratory and cardiovascular systems (Pope III and Dockery, 2006; Tie et al., 2009; Chen et al., 2013; Xu et al., 2013), but also influences vehicular traffic and crop yields (Chameides et al., 1999; Wu et al.,

50 | 2005). As a result, haze pollution has received considerable attention from ~~both~~ the government
51 | and the public. Unfortunately, on the one hand, overwhelming industrialization leads to more
52 | severe haze contamination over the Beijing–Tianjin–Hebei (BTH) region (~~Yin et al., 2015~~ Xu et
53 | al., 2015); whilst on the other hand, the trumpet-shaped topography (Fig. 1) of the region is
54 | unfavorable for the dissipation of air pollution, thus making the BTH region home to some of the
55 | worst haze weather in China. Since the BTH region is the most economically developed region in
56 | North China and is at the heart of Chinese politics and culture (~~not least because it is home to the~~
57 | ~~capital city, Beijing, and Xiongan New Area, for instance~~), severe haze pollution in this region has
58 | become a critical issue (e.g., Mu and Zhang, 2014; ~~Yin et al., 2015~~; Wang, 2018), especially since
59 | the occurrence of the unprecedented severe haze event in North China in January 2013 (Wang et
60 | al., 2014; Zhang et al., 2014; Mu and Zhang, 2014; Tao et al., 2014; Zhang et al., 2015).

61 | To date, numerous efforts have been made to explore the causes of wintertime haze pollution over
62 | the BTH region and its surroundings, and these ~~efforts~~ previous studies roughly fall into three
63 | categories ~~of results from based on~~ the climatological perspective. The first category ~~features~~
64 | ~~studies that have reported reports~~ that the joint effects of the emissions of various sources of APs
65 | (e.g., Cao et al., 2007; Guo et al., 2011; Zhu et al., 2016) and climate anomalies (e.g., Chen and
66 | Wang, 2015; Wang and Chen, 2016; Yin and Wang, 2016a; Cai et al., 2017; ~~Yin et al., 2017~~; Yin
67 | and Wang, 2018; Wang, 2018) may have brought about the increasing severity of haze pollution
68 | over China in recent decades. The second category of studies, meanwhile, underlines the causality
69 | of the variation in winter haze days in eastern and northern China from the perspective of climate
70 | anomalies (e.g., Li et al., 2016; Yin and Wang, 2016b; ~~Yin and Wang, 2018~~; Pei et al., 2018). For
71 | instance, it is suggested that a weakened East Asian winter monsoon (EAWM) system ~~has been~~
72 | ~~suggested as being responsible for could lead to the~~ above-normal numbers of winter haze days
73 | (e.g., Niu et al., 2010; Li et al., 2016; Yin and Wang, 2016a; ~~Yin and Wang, 2017~~; Yin et al.,
74 | 2017); ~~plus~~ Meanwhile, the variability of EAWM's ~~variability~~ has been shown to be
75 | significantly tied to the East Atlantic–West Russia pattern (~~Yin et al., 2017~~; ~~Yin and Wang, 2017~~)
76 | and Eurasian pattern (Zhang et al., 2016; ~~Yin et al. and Wang, 2017~~). The third category ~~of studies~~
77 | focuses on the external forcings associated with the variability of winter haze days. These forcings
78 | include the sea surface temperature (SST) (e.g., Gao and Li, 2015; Wang et al., 2015; ~~Yin and~~
79 | ~~Wang, 2016a~~; Yin et al., 2017), Arctic sea ice (e.g., Wang et al., 2015; Zou et al., 2017), Eurasian
80 | snowpack (e.g., Yin and Wang, and Wang, 2017; ~~Yin and Wang, 2018~~), and the thermal conditions
81 | on the Tibetan Plateau (e.g., Xu et al., 2016). However, most of these previous works have focused
82 | on wintertime, with little attention having been paid to other seasons.

83 | Autumn is a transitional season from the wet and hot ~~conditions of~~ summer to the dry and cold
84 | ~~conditions of~~ winter. Climatologically, ~~T~~ the weather in autumn over the BTH region is
85 | ~~climatologically~~ quite pleasant, with favorable temperatures and light winds. Outdoor activities
86 | and tourism are therefore prevailing important, economically, in the autumn season. However,
87 | ~~notably,~~ autumn is also a season in which haze weather frequently occurs in the BTH region
88 | (Chen and Wang, 2015), ~~and~~ ~~†~~ The number of autumnal haze days (AHDs) has increased
89 | remarkably in recent years. Such an increase in the number of haze days is a potential threat to ~~the~~
90 | ~~outdoor activities and~~ tourism economics in this region ~~that, as mentioned, are so important to the~~
91 | ~~region at this time of year~~. Therefore, research into the causes of the interannual variation in
92 | AHDs in the BTH region (AHD_{BTH}) is imperative. Such work not only provides scientific support
93 | to the year-to-year scheduling of anthropogenic emissions for dealing with autumnal haze
94 | pollution, but also helps the government with facilitating the arrangement of tourism
95 | ~~economic~~ tourism and outdoor activities. However, ~~as already mentioned,~~ compared to the myriad
96 | publications studies on wintertime haze pollution, autumn haze pollution over the BTH region has
97 | attracted far less attention, with only a few case studies on atmospheric circulation having been

98 reported (Yang et al., 2015; Gao and Chen, 2017; Wang et al., 2018). It was this knowledge gap
99 that motivated us to revisit the variability of AHD_{BTH} . Considering that the SST acts as a crucial
100 driver of large-scale climate variability (e.g., Wang et al., 2009; Zhu et al., 2014; He and Zhu,
101 2015; Xiao et al., 2015; Zhu and Li, 2017; Zhu, 2018), we aimed to figure out the underlying air-
102 sea interaction mechanisms for the interannual AHD_{BTH} variability in the present study.

103 The remainder of this paper is organized as follows. Section 2 introduces the data, model and
104 methodology. Section 3 presents the atmospheric anomalies associated with AHD_{BTH} . Section 4
105 addresses the mechanisms ~~and pathways of~~ how remote SST anomalies (SSTAs) ~~in driving~~ the
106 interannual variations of AHD_{BTH} . Conclusions and further discussion are provided in the final
107 section.

108

109 **2 Data, model and methodology**

110

111 **2.1 Data**

112 The data used in this study are as follows: (1) monthly mean planetary boundary layer height
113 (PBLH), with a $1^\circ \times 1^\circ$ horizontal resolution, from the European Centre for Medium-Range
114 Weather Forecasts Interim Reanalysis (ERA-Interim) (Dee et al., 2011); (2) monthly mean
115 atmospheric data, with a $2.5^\circ \times 2.5^\circ$ horizontal resolution, ~~from the National Centers for~~
116 ~~Environmental Prediction (NCEP) National Center for Atmospheric Research (NCAR)~~
117 ~~Reanalysis I (NCEP/NCAR) (Kalnay et al., 1996);~~ and total cloud cover (entire atmosphere
118 considered as a single layer; 192×94 points in the horizontal direction), ~~also from NCEP/NCAR~~
119 ~~from the National Centers for Environmental Prediction (NCEP)–National Center for Atmospheric~~
120 ~~Research (NCAR) Reanalysis I (NCEP/NCAR) (Kalnay et al., 1996);~~ (3) monthly mean SST, with
121 a $2^\circ \times 2^\circ$ horizontal resolution, of the Extended Reconstructed SST dataset, version 5 (ERSST.v5;
122 Huang et al., 2017), from the National Oceanic and Atmospheric Administration (NOAA); (4)
123 global monthly precipitation data, with a $2.5^\circ \times 2.5^\circ$ horizontal resolution, from NOAA's
124 precipitation reconstruction (Chen et al., 2002); (5) ground-timing observation datasets, at 02:00,
125 08:00, 14:00 and 20:00 BLT (Beijing local time), from the National Meteorological Information
126 Center of China. The temporal coverage of the PBLH data is from 1979 to 2017, while the
127 remaining datasets are from 1960 to 2017. Here, boreal autumn refers to the seasonal mean for
128 September–October–November (SON).

129

130 **2.2 Model**

131 The numerical model ~~used here we employed~~ is an anomaly atmospheric general circulation
132 model (AGCM) based on the Geophysical Fluid Dynamics Laboratory (GFDL) global spectrum
133 dry AGCM (Held and Suarez, 1994), ~~which is employed to investigate the mechanisms for the~~
134 ~~atmospheric responses to the specified SST-induced heating.~~ The horizontal resolution is T42,
135 with five evenly spaced sigma levels ($\sigma = p/ps$; interval: 0.2; top level: $\sigma = 0$; bottom level: $\sigma = 1$).
136 A realistic autumn mean state, obtained from the long-term mean of the NCEP/NCAR reanalysis
137 data, is prescribed as the model basic state. This model has been used to unravel the eddy-mean
138 interaction over East Asia and its downstream climate impacts ~~on over~~ North America ~~n climate~~
139 (Zhu and Li, 2016, 2018).

140

141

142

143 2.3 Methodology

144 The definition of a haze day in the present study is identical to ~~that used in the~~ previous studies
145 (~~e.g.,~~ Chen and Wang, 2015; ~~Yin et al., 2017; Pei et al., 2018~~). ~~It, which~~ is based on the
146 ground-timing observations of relative humidity, visibility and wind speed. It is important to point
147 out that the visibility observations switched from manual to automatic in 2014, and the visibility
148 threshold for haze was thus also slightly modified from then on. ~~Nevertheless~~ ~~However~~, the
149 continuity of the data was not affected. Following Zhang et al. (2016), the mean number of haze
150 days ($\overline{\text{NHD}}$) for AHD_{BTH} was computed by:

$$151 \quad \overline{\text{NHD}} = \frac{1}{n} \sum_{i=1}^n N \quad (1)$$

152 where n (here, $n = 20$) is the number of meteorological sites distributed within the BTH region
153 (Fig. 1), and N denotes the number of haze days at a site for each autumn.

154 Similar to the approach proposed by Zhu and Li (2017), the 9-yr running mean of the AHD_{BTH}
155 was used to represent the interdecadal component of the AHD_{BTH} , whereas the interannual
156 component was obtained by removing the interdecadal component from the raw AHD_{BTH} . Since
157 there is a tapering problem when calculating the running mean, the first four years and the last
158 four years of the interdecadal component of the AHD_{BTH} could be estimated by the mean value of
159 the available data with a shorter window. For example, the interdecadal component of the AHD_{BTH}
160 for 2016 and 2017 could be obtained by the mean of 2012–17 and 2013–17, respectively. Note
161 that the temporal correlation coefficients (TCCs) between the AHD_{BTH} and every single
162 ~~stationsite~~ were all positive and significant (Fig. 1), indicating ~~the~~ coherency ~~in of~~ the interannual
163 variability of ~~autumnal~~ haze days ~~in each station~~ over the BTH region; ~~plus~~ ~~meanwhile~~, the
164 distribution of these ~~sites~~ ~~stations~~ was ~~also~~ fairly even. Therefore, the interannual component of
165 the AHD_{BTH} could be ~~used as a~~ good representation of the year-to-year pollution state over the
166 whole BTH region in autumn.

167 Linear regression, composite analysis and correlation were used to examine the ~~associated~~
168 circulation and SSTAs ~~that associated with the interannual~~ AHD_{BTH} . The two-tailed Student's
169 t -test was employed to evaluate the statistical significance of these analyses. The wave activity
170 flux (WAF; Takaya and Nakamura, 2001) was calculated to depict the tendency of Rossby wave
171 energy propagation.

173 3 Atmospheric anomalies associated with the interannual changes of AHD_{BTH}

174 Figure 2 illustrates the time series of the raw AHD_{BTH} , along with its interdecadal and interannual
175 components. A prominent feature is that the AHD_{BTH} displays both interannual and interdecadal
176 variability. On the interdecadal timescale, the AHD_{BTH} was below average during 1960–1975 and
177 the late-2000s, but above average during 1975–2003, and it increased dramatically after 2009. On
178 the interannual timescale, the AHD_{BTH} presents large differences year ~~on by~~ year. For example, the
179 AHD_{BTH} was at its lowest in 2012, but peaked in 2014. Since the interannual variability explains
180 most of the ~~total~~ variances in the AHD_{BTH} variability, in this study we ~~only~~ investigate the
181 atmospheric anomalies and unravel the underlying physical ~~processes mechanisms and pathways~~
182 ~~associated that associated~~ with the AHD_{BTH} on the interannual timescale.

183 Close scrutiny of the large-scale and localized dynamic and thermodynamic fields associated with
184 the AHD_{BTH} ~~should help in could~~ ~~advancing~~ our understanding of the ~~possible~~ underlying

185 mechanisms. In this regard, we firstly examine the climatological mean autumnal 500-hPa
186 geopotential height (Z500), 850-hPa winds (UV850) and total cloud, along with the surface
187 relative humidity and surface air temperature that potentially impact the climate over the BTH
188 region (Fig. 3). There is a shallow mid-tropospheric trough over coastal East Asia (Fig. 3a), which
189 resembles the trough in winter (Zhao et al., 2018; Pei et al., 2018) but with a smaller magnitude.
190 Behind the trough, a clear anticyclonic circulation appears over the central-eastern China, with
191 remarkable westerly/northwesterly winds dominating the BTH region (Fig. 3a). ~~Cold-Cool~~ and dry
192 air from higher latitudes is advected by the winds, and the BTH region is thus much cooler and
193 drier and has less cloud than other regions at the same latitudes (e.g., the central ~~portion of~~ Japan).
194 As such, the autumnal BTH region features breezy and windy conditions ~~climatologically~~, with
195 low surface relative humidity (Fig. 3b), reducing the likelihood of haze there via the effect of cold
196 advection ~~and~~ ventilation. Note, however, that if the breezy conditions are interrupted, haze
197 pollution ~~may be enhanced~~ is likely to occur. One may ask whether a higher AHD_{BTH} is related to
198 the interference of such breezy conditions. Figures 4 and 5 were therefore plotted to examine the
199 associated atmospheric parameters/circulations. For simplicity, the regression and composite
200 analyses in this study reported hereafter are interpreted with respect to positive phase of AHD_{BTH}
201 anomalies only.

202 Previous studies have revealed that haze pollution is closely correlated with local meteorological
203 parameters in the planetary boundary layer (e.g., You et al., 2017; Chen et al., 2018). Figure 4
204 suggests that an above-normal AHD_{BTH} is tied to a localized ~~increase enhancement~~ of surface
205 relative humidity (Fig. 4a) and surface air temperature (Fig. 4b), along with ~~decrease of~~ suppressed
206 surface wind speed (Fig. 4c), sea-level pressure (SLP) (Fig. 4d) and PBLH (Fig. 4e). ~~Specifically,~~
207 it seems that autumnal haze pollution is more significantly correlated with temperature and PBLH.
208 The question is ~~So~~, what causes the above anomalous parameters that are favorable for a higher
209 AHD_{BTH}?

210 Figure 5 shows the associated large-scale atmospheric circulation anomalies at different levels of
211 troposphere. ~~From~~ In Figs. 5a–5d, the most noticeable feature is that there is a planetary-scale,
212 quasi-barotropic Rossby wave train emanating from the North Atlantic subtropical sector. In
213 addition to an anticyclonic anomaly centered over the North Atlantic subtropics, this
214 teleconnection pattern has another two pairs of anomalous cyclones (low pressure) and
215 anticyclones (high pressure) stretching across Eurasia to the ~~North Pacific~~ Northeast Asia, i.e., a
216 cyclonic anomaly centered over the ocean south of Greenland, an anticyclonic anomaly centered
217 over Scandinavia, a cyclonic anomaly centered over the adjacent central Siberia, and an Northeast
218 Asian anticyclonic anomaly centered over the Sea of Japan (SJ). In general, based on the regressed
219 atmospheric fields, the teleconnection has a much larger amplitude in the upper troposphere (Fig.
220 5a), ~~rather than that~~ in the mid-troposphere (Fig. 5b) and lower troposphere (Fig. 5c). Intriguingly,
221 from the surface projection of the above quasi-barotropic teleconnection pattern, we can discern a
222 positive phase of North Atlantic Oscillation -like mode in connection with this pattern (Hurrell and
223 Deser, 2009).

224 Among all the height anomalies within the teleconnection, the anomalous quasi-barotropic
225 Northeast Asian anticyclonic anomaly centered over the SJ (A_{SJ}) plays a direct role in driving a
226 higher AHD_{BTH}. The related ~~physical~~ physico-meteorological causes are as follows: There are
227 southerly/southeasterly anomalies along the western flank of the A_{SJ} in the lower troposphere (Figs.
228 5c and 5d), manifesting the capability of suppressed atmospheric horizontal diffusion and thus
229 favoring a buildup of substantial local and nonlocal APs and warmer moisture over the BTH
230 region (Yang et al., 2015; Yang et al., 2016) under the specific topographical forcing of the
231 Taihang Mountains and Yan Mountains (Fig. 1). On the other hand, the significant positive

232 pressure anomaly in the mid-to-upper parts of the A_{SJ} (Figs. 5a and 5b) not only impedes the
233 intrusion of cold air into the BTH region, but also facilitates consistent air subsidence over the
234 BTH region and its surrounding areas (Fig. 4f), resulting in the decrease of the PBLH and
235 ~~increase~~ amplification of static stability (i.e., the dampened vertical dispersion of the atmosphere).
236 Consequently, the meteorological conditions connected to a higher AHD_{BTH} are ~~adverse to quite~~
237 ~~different from~~ the autumnal mean climate state ~~climatological characteristics~~ (Fig. 3).

238 To summarize, the A_{SJ} and the associated subsidence can induce the capacity for suppressed local
239 horizontal and vertical dispersion over the BTH region and its surrounding areas, as shown in the
240 above-mentioned anomalous parameters ~~in the boundary layer~~ (Fig. 4); and these parameters are
241 further responsible for the accumulation and secondary formation/hygroscopic growth of APs
242 (Jacob and Winner, 2009; Ding and Liu, 2014; Mu and Liao, 2014; Jia et al., 2015). As such, the
243 haze pollution over the BTH region is readily established within a narrow space. ~~Therefore, The~~
244 ~~the~~ question of how the above-normal AHD_{BTH} is stimulated could plausibly be transferred into
245 ~~questioning the pathways of~~ how the A_{SJ} is developed and sustained. In fact, the A_{SJ} and the
246 associated air subsidence are modulated by remote SSTAs. We tackle the underlying
247 ~~mechanisms~~ this issue in the next section.

248

249 ~~4 Possible m~~ Mechanisms for the A_{SJ} and pathways

250

251 4.1 Observational diagnoses

252 Figure 5c shows that an above-normal AHD_{BTH} is closely correlated with SST warming in two key
253 regions: One is the North Atlantic subtropical sector ($R1: 22^{\circ}\text{--}32^{\circ}\text{N}, 90^{\circ}\text{--}40^{\circ}\text{W}$), and the other is
254 the western North Pacific sector ($R2: 10^{\circ}\text{--}30^{\circ}\text{N}, 108^{\circ}\text{--}140^{\circ}\text{E}$), with its southern portion belonging
255 to the Western Pacific Warm Pool (You et al., 2018). One may ask why we chose these two key
256 SSTA regions. Firstly, the subtropical North Atlantic is the only region over North Atlantic that
257 highly correlated with the AHD_{BTH} on interannual timescale. Although the regression SSTA
258 pattern over North Atlantic looks like a tri-pole SST pattern which has profound impacts on
259 Eurasian climate (e.g., Zuo et al., 2013), the relationship between AHD_{BTH} and simultaneous
260 North Atlantic Tripole (NAT) SST pattern is insignificant. The correlation coefficient between
261 AHD_{BTH} and NAT SST index (Deser and Michael, 1997) is only 0.17. Therefore, we chose the
262 middle oceanic region of North Atlantic as the key region for AHD_{BTH} . Secondly, the positive
263 correlated SSTA over R1 and R2 region can both induce positive rainfall anomaly (diabatic
264 heating; Figs 5e, 9b), the SSTAs should play an active role in local air-sea interaction and in turn
265 influence the large-scale circulation. Therefore, we chose the R1 and R2 as the key SSTA regions
266 from both statistical diagnosis and physical basis. Meanwhile, from Fig. 5e we can discern that
267 enhanced and significant precipitation appears to the north of R1, indicating an active atmospheric
268 response to the SST warming over R1; whereas, there is an insignificant positive precipitation
269 signal over R2 and its surrounding areas. Figure 6 further depicts that the SON SSTs over both R1
270 and R2 are positively correlated with AHD_{BTH} , and the TCC between the AHD_{BTH} and SON SST
271 over R1 (R2) is 0.45 (0.28), exceeding the 99% (95%) confidence level. By virtue of the above
272 analyses, we speculate that the SST over R1 may play a more important role than that over R2 in
273 driving a higher AHD_{BTH} . Note, however, that when the SON SSTs over R1 and R2 are both
274 obviously elevated, the AHD_{BTH} is more likely to be higher than normal, such as in 1980, 1987
275 and 2015. ~~Furthermore, a~~ A_{SJ} indicated above, the AHD_{BTH} is closely correlated with the A_{SJ} and
276 the associated air subsidence, which allows us to speculate that the positive SSTAs over R1 and
277 R2 might drive the interannual variability of AHD_{BTH} by modulating the intensity of the A_{SJ} and
278 associated subsidence. To validate this hypothesis, we firstly examine the pathway of SSTAs over

279 R1 in driving AHD_{BTH} .

280 Figure 5c suggests that the SST warming in R1 may induce larger-area ~~concomitant~~ low-level
281 easterly anomalies ~~to its east, leading to anticyclonic wind shear over this region, which mainly~~
282 ~~form over the southeastern portion of R1 and the area to its south~~. In such a scenario, an
283 anticyclonic anomaly is induced (Fig. 5c), with its center to the northeast of R1. Along the western
284 flank of this anticyclonic anomaly, warm and moist airflows move northwards. When these warm
285 and moist airflows meet cold air mass in the areas to the north of R1, enhanced precipitation is
286 thus generated (Fig. 5e). Meanwhile, the resultant enhanced rainfall condensation heating induces
287 a cyclonic anomaly to its north, thereby exciting the other two pairs of the aforementioned
288 teleconnection pattern along the westerly jet, as demonstrated by the Rossby wave train induced
289 by SST warming in R1 (Figs. 7 and 8). Specifically, from the regressed SON UV850 (Fig. 7), we
290 can see that the SST warming in R1 can indeed induce a significant low-level teleconnection
291 pattern arising from the North Atlantic subtropics, bearing a close resemblance to that in Fig. 5c;
292 and to the north of R1, where the rainfall condensation heating is triggered, the corresponding
293 WAF exhibits a distinctive arc-shaped trajectory, perturbing the other two pairs of cyclones and
294 anticyclones of the teleconnection (Fig. 8). This teleconnection extends from the North Atlantic
295 towards Scandinavia, goes through the Eurasia and arrives at the ~~Northeast Asia~~~~western North~~
296 ~~Pacific~~. Therefore, by means of this trajectory, Rossby wave energy in the middle (Fig. 8b) and
297 upper (Fig. 8a) troposphere may propagate southeastwards into the A_{SJ} and its surrounding region,
298 favoring the formation/sustainability of the A_{SJ} and the associated air subsidence. In this context,
299 the associated meteorological parameters (Fig. S1), which resemble those tied to a higher AHD_{BTH}
300 (Fig. 4), might increase the likelihood of SON haze pollution over the BTH region. Again, this
301 induced teleconnection is quasi-barotropic in structure, with its magnitude larger in the upper
302 troposphere (Fig. 8a), which is consistent with that in Fig. 5a.

303 ~~As for the role of~~~~When focusing on region~~ R2 SST warming (Fig. 9a), we find that, corresponding
304 to the SSTAs over R2, there exists a cyclonic anomaly to the west of R2. Besides, substantial
305 SSTA-induced low-level easterly anomalies are ~~appeared to mainly located to~~ the southeast of R2;
306 ~~meanwhile~~~~plus~~, a ~~large-scale~~~~huge~~ anticyclonic anomaly to the northeast is excited, with its center
307 situated over the northern Pacific. In such a scenario, R2 is thoroughly ~~controlled~~~~penetrated~~ by
308 significant warm and humid airflows transported from the eastern flank of the cyclonic and the
309 western flank of anticyclonic anomaly respectively (Fig. 9a), ~~warming the SST over R2~~.
310 Furthermore, the airflow convergence primarily occurs over the southwestern portion of R2,
311 where the strongly significant and positive rainfall anomaly is triggered (Fig. 9b). Thus, the
312 enhanced significant rainfall heating ~~perturbation~~ may greatly intensify the ascending motion over
313 R2 and the adjacent region, resulting in subsidence over the BTH region and Northeast Asia via an
314 anomalous local meridional cell (Fig. 10a). As such, the BTH region ~~and its adjacent areas are~~
315 ~~dominated by significant warm temperatures in the middle and upper troposphere (Fig. 10b),~~
316 ~~leading to the maintenance and reinforcement of the A_{SJ} and the downward motions over the BTH~~
317 ~~region, as well as the regional low-level stability. Accordingly, the A_{SJ} , the downward motions as~~
318 ~~well as the low-level stability over the BTH region, are well maintained and reinforced~~. Under
319 such circumstances, the vertical transport of APs is restricted (Zhang et al., 2014; Pei et al., 2018),
320 and the near-surface winds are weakened (Li et al., 2016). ~~Meanwhile,~~ ~~†~~ The parameters associated
321 with SST warming in R2 (Fig. S2) also support the formation of haze weather over the BTH
322 region.

323

324 4.2 Numerical model simulations

325 Two experiments were conducted to further validate the above-mentioned two pathways ~~in of~~ how

326 SSTAs drive the variation of AHD_{BTH} . The first experiment (H_NAS) simulated the responses to
327 the heating induced by SSTAs over R1 (Fig. 11). H_NAS was imposed with a specified heating
328 centered over the region to the north of R1 (center: $37.67^{\circ}N$, $64.69^{\circ}W$) that largely matched with
329 the SON positive rainfall anomaly as shown in Fig. 5e. The second experiment (H_WNP)
330 mimicked the responses to the prescribed heating over the neighboring areas of R2 (center:
331 $15.35^{\circ}N$, $109.69^{\circ}E$; Fig. 12), where the corresponding regressed precipitation rate was the most
332 significant ~~and amplified~~, as exhibited in Fig. 9b. The heating had a cosine-squared profile in an
333 elliptical region in the horizontal direction. The maximum heating, with 1 K day^{-1} amplitude, was
334 set to be at 300 hPa.

335 Figure 11 presents the 200- and 500-hPa geopotential height and wind responses to the specified
336 heating over the North Atlantic subtropical region. As anticipated, the equilibrium state (mean
337 output from day 40 to day 60) of the Z200 (Fig. 11a) and Z500 (Fig. 11b) responses to the heating
338 resembles the aforementioned teleconnection (Figs. 5a and 5b), and the simulated response of the
339 Z200 anomalies is generally larger than its counterpart at 500 hPa (Fig. 11b), which concurs with
340 the observational evidence. Besides, a similar low-level portion of the A_{SJ} could also be simulated
341 (figure not shown). As a result, a strengthened A_{SJ} is induced.

342 Figure 12 delineates the 850-hPa geopotential height (Z850) and UV850 responses to the specified
343 heating centered at ($15.35^{\circ}N$, $109.69^{\circ}E$). Although there are some differences in spatial
344 distribution compared with the observations, the well-organized cyclonic anomaly to the west of
345 the heating center and the anticyclonic anomaly ~~over Northeast Asia to the north~~ can be ~~properly~~
346 well simulated (Fig. 12). Meanwhile, the A_{SJ} and the coherent tropospheric subsidence over the
347 BTH region and the Northeast Asian anticyclonic anomaly were also simulated well (figure ~~not~~
348 shown~~omitted~~), ~~leading to the amplified A_{SJ} as well.~~

349 To sum up, from observational diagnoses and numerical simulations, we can conclude that there
350 are two pathways regarding how remote SSTAs impact the formation and maintenance of the A_{SJ}
351 and the associated air subsidence. One pathway operates via a heating-induced large-scale
352 teleconnection pattern arising from SST warming in R1, and the other is connected to an
353 anomalous local meridional cell triggered by heating-reinforced ascending motion via local SST
354 warming over R2.

355

356

357 **5 Conclusions and discussion**

358 Motivated by a lack of in-depth understanding with respect to the interannual variations of the
359 AHD_{BTH} , in the present study we explored the related climate anomalies (localized meteorological
360 parameters, and large-scale atmospheric and oceanic anomalies) tied to the AHD_{BTH} . We have
361 substantiated that an above-normal AHD_{BTH} is closely correlated with the simultaneous SST
362 warming in two key regions (R1 over the North Atlantic subtropical sector, and R2 over the
363 western North Pacific sector), and once the SON SST warming in R1 and R2 are both remarkably
364 significant, their joint climate impacts can greatly enhance the likelihood of an above-normal
365 AHD_{BTH} .

366 Potential mechanisms associated with an above-normal AHD_{BTH} have been proposed through
367 further investigations. Since the A_{SJ} and the associated subsidence over the A_{SJ} and the
368 surrounding region can yield meteorological circumstances conducive to enhancing the likelihood
369 of haze pollution in the BTH region, the issue of an above-normal AHD_{BTH} can be reasonably
370 transferred into uncovering how the SON A_{SJ} and associated air subsidence are developed and

371 sustained. We found that there are two possible pathways. First, SST warming in R1 can induce a
372 downstream Rossby wave teleconnection, and the associated Rossby wave energy can propagate
373 into ~~Northeast Asia~~ ~~A_{SJ}~~ ~~and its surrounding region~~ through an arc-shaped trajectory,
374 developing and strengthening the A_{SJ} and the associated subsidence over the BTH region. The
375 other pathway, however, operates through localized heating-reinforced ascending motion over R2,
376 also resulting in subsidence over the BTH region ~~and Northeast Asia~~ via an anomalous local
377 meridional cell.

378 AGCM simulations ~~supported~~ ~~reinforced~~ our hypothesis. With prescribed heating over the region
379 to the north of R1, a quite similar teleconnection—starting from the North Atlantic
380 subtropics—was excited. If we imposed an idealized heating over the adjacent R2, where the
381 corresponding precipitation rate was the most significant ~~and amplified~~, the ~~concomitant~~
382 significant low-level convergence around the heated areas was simulated, ~~enhancing the SST~~
383 ~~warming in R2~~ and inducing the A_{SJ} -resembled circulation to the north and the subsidence over
384 the BTH region ~~and Northeast Asia~~. However, because the model we used is an intermediate
385 anomaly AGCM, and the heating prescribed in the model is idealized, the simulated patterns were
386 slightly spatially different to those observed. Although the model cannot reproduce the
387 geopotential height and wind anomalies perfectly, it can ~~nonetheless still~~ support ~~the our~~ proposed
388 mechanisms. As a summary, a schematic illustration (Fig. 13) of the occurrence of a higher
389 AHD_{BTH} is provided, which encapsulates the major characteristics of the two pathways of how
390 ~~remote~~ SSTAs over R1 and R2 drive the AHD_{BTH} respectively.

391 From the perspective of seasonal prediction, among all the previous individual months of boreal
392 summer (June–July–August), the SON SST in R1 (R2) was most significantly correlated with the
393 August SST in R1 (R2) on the interannual timescale, with a TCC of 0.35 (0.61) that exceeded the
394 95% (99%) confidence level. This suggests that, when the August SST over R1 (R2) is higher, the
395 subsequent SON SST over R1 (R2) is more likely to become warmer. As such, the previous
396 August SSTA over R1 (R2) could serve as a possible precursor for the seasonal prediction of the
397 AHD_{BTH} .

398 In this study, we solely emphasize the potential impacts of SSTAs on the interannual variations of
399 the AHD_{BTH} . It should be noted that other external forcings, such as the Arctic sea ice (e.g., Wang
400 et al., 2015), Eurasian snowpack (e.g., Yin and Wang, 2018), thermal conditions on the Tibetan
401 Plateau (e.g., Xu et al., 2016) and soil moisture (e.g., Yin and Wang, 2016b), may also exert
402 profound impacts on haze pollution over China. Studying the mechanisms tied to these forcings
403 may enhance the seasonal predicting skill for the AHD_{BTH} . Meanwhile, in this study, we only
404 focus on the variability of AHD_{BTH} on interannual timescale. Whether the proposed mechanism of
405 AHD_{BTH} is still at play on intraseasonal timescale? Is it possible for making an extended-range
406 forecast of the occurrence of haze days? ~~This-These is an important~~ topics are of both scientific
407 and practical importance, and merit ~~deserving of~~ further explorations.

410 *Data availability.* The atmospheric data and land-surface data are available from the NCEP/NCAR data archive:
411 <http://www.esrl.noaa.gov/psd/data/gridded/data.ncep.reanalysis.html> (NCEP/NCAR, 2018). The SST data were downloaded from
412 <https://www.esrl.noaa.gov/psd/data/gridded/data.noaa.ersst.v5.html> (NOAA, 2018). The precipitation data were downloaded from
413 <https://www.esrl.noaa.gov/psd/data/gridded/data.prec.html> (NOAA, 2018). The monthly PBLH data are available on the ERA-Interim
414 website: <http://www.ecmwf.int/en/research/climate-reanalysis/era-interim> (ERA-Interim, 2018). The ground observations are from the
415 National Meteorological Information Center of China (<http://data.cma.cn/>) (CMA, 2018).

416 *Competing interests.* The authors declare that they have no conflict of interest.

417 *Author contributions.* JW analyzed the observational data, ZZ and JW designed the numerical experiments. JW and ZZ wrote the
418 manuscript. LQ, QZ, JH and JXW were involved in the scientific interpretation and discussion.

419

420 *Acknowledgements.* This work was supported by the National Key Research and Development Program of China (Grants
421 2018YFC1505905 and 2018YFC1505803), and the National Natural Science Foundation of China (Grants 41605035, 41371222, and
422 41475086) and the Priority Academic Program Development (PAPD) of Jiangsu Higher Education Institutions. Zhiwei was supported by
423 the Natural Science Foundation of Jiangsu Province (No. BK20161604) and the Startup Foundation for Introducing Talent of NUIST (No.
424 2018r026).

425

426

427

428

429

430

431

432

433

434

435

436

437

438

439

440

441

442

443

444

445

446

447

448

449

450

451

452

453

454

455

456

457

458

459 **References**

- 460 Cai, W. J., Li, K., Liao, H., Wang, H. J., and Wu, L. X.: Weather conditions conducive to Beijing severe haze more
461 frequent under climate change, *Nat Clim Change*, 7, 257-262, 10.1038/nclimate3249, 2017.
- 462 Cao, J. J., Lee, S. C., Chow, J. C., Watson, J. G., Ho, K. F., Zhang, R. J., Jin, Z. D., Shen, Z. X., Chen, G. C., Kang,
463 Y. M., Zou, S. C., Zhang, L. Z., Qi, S. H., Dai, M. H., Cheng, Y., and Hu, K.: Spatial and seasonal distributions
464 of carbonaceous aerosols over China, *J Geophys Res Atmos*, 112, D22S11, 10.1029/2006JD008205, 2007.
- 465 Chameides, W. L., Yu, H., Liu, S. C., Bergin, M., Zhou, X., Mearns, L., Wang, G., Kiang, C. S., Saylor, R. D., Luo,
466 C., Huang, Y., Steiner, A., and Giorgi, F.: Case study of the effects of atmospheric aerosols and regional haze on
467 agriculture: An opportunity to enhance crop yields in China through emission controls?, *Proceedings of the*
468 *National Academy of Sciences*, 96, 13626, 1999.
- 469 Charlson, R. J., Schwartz, S. E., Hales, J. M., Cess, R. D., Coakley Jr, J. A., Hansen, J. E., and Hofmann, D. J.:
470 Climate forcing by anthropogenic aerosols, *Science*, 255, 423-430, 10.1126/science.255.5043.423, 1992.
- 471 Chen, H. P., and Wang, H. J.: Haze Days in North China and the associated atmospheric circulations based on daily
472 visibility data from 1960 to 2012, *J Geophys Res Atmos*, 120, 5895-5909, 10.1002/2015JD023225, 2015.
- 473 Chen, J., Zhao, C. S., Ma, N., Liu, P. F., Göbel, T., Hallbauer, E., Deng, Z. Z., Ran, L., Xu, W. Y., Liang, Z., Liu, H.
474 J., Yan, P., Zhou, X. J., and Wiedensohler, A.: A parameterization of low visibilities for hazy days in the North
475 China Plain, *Atmos Chem Phys*, 12, 4935-4950, 10.5194/acp-12-4935-2012, 2012.
- 476 Chen, M. Y., Xie, P. P., Janowiak, J. E., and Arkin, P. A.: Global land precipitation: A 50-yr monthly analysis based
477 on gauge observations, *J Hydrometeorol*, 3, 249-266, 10.1175/1525-7541(2002)003<0249:glpaym>2.0.co;2, 2002.
- 478 Chen, Y. N., Zhu, Z. W., Luo, L., and Zhang, J. W.: Severe haze in Hangzhou in winter 2013/14 and associated
479 meteorological anomalies, *Dyn Atmos Oceans*, 81, 73-83, 10.1016/j.dynatmoce.2018.01.002, 2018.
- 480 Chen, Y. Y., Ebenstein, A., Greenstone, M., and Li, H. B.: Evidence on the impact of sustained exposure to air
481 pollution on life expectancy from China's Huai River policy, *Proc Natl Acad Sci*, 110, 12936-12941,
482 10.1073/pnas.1300018110, 2013.
- 483 Chen, Z. Y., Xie, X. M., Cai, J., Chen, D. L., Gao, B. B., He, B., Cheng, N. L., and Xu, B.: Understanding
484 meteorological influences on PM_{2.5} concentrations across China: a temporal and spatial perspective, *Atmos*
485 *Chem Phys*, 18, 5343-5358, 10.5194/acp-18-5343-2018, 2018.
- 486 Chung, C. E., Ramanathan, V., and Kiehl, J. T.: Effects of the South Asian absorbing haze on the Northeast
487 monsoon and surface-air heat exchange, *J Climate*, 15, 2462-2476,
488 10.1175/1520-0442(2002)015<2462:eotsaa>2.0.co;2, 2002.
- 489 CMA: China ground observation data sets, available at: <http://data.cma.cn/>, last access: 10 January 2018 (in
490 Chinese).
- 491 Dee, D. P., Uppala, S. M., Simmons, A. J., Berrisford, P., Poli, P., Kobayashi, S., Andrae, U., Balmaseda, M. A.,
492 Balsamo, G., Bauer, P., Bechtold, P., Beljaars, A. C. M., van de Berg, L., Bidlot, J., Bormann, N., Delsol, C.,
493 Dragani, R., Fuentes, M., Geer, A. J., Haimberger, L., Healy, S. B., Hersbach, H., Hólm, E. V., Isaksen, I.,
494 Kållberg, P., Köhler, M., Matricardi, M., McNally, A. P., Monge-Sanz, B. M., Morcrette, J. J., Park, B. K.,
495 Peubey, C., de Rosnay, P., Tavolato, C., Thépaut, J. N., and Vitart, F.: The ERA-Interim reanalysis: configuration
496 and performance of the data assimilation system, *Q J R Meteorol Soc*, 137, 553-597, 10.1002/qj.828, 2011.
- 497 Deser, C. and Michael S.T.: Atmosphere-ocean interaction on weekly timescales in the North Atlantic and Pacific.
498 *Journal of Climate*, 10(3): 393-408, 1997.

499 Ding, Y. H., and Liu, Y. J.: Analysis of long-term variations of fog and haze in China in recent 50 years and their
500 relations with atmospheric humidity, *Sci China Earth Sci*, 57, 36-46, 10.1007/s11430-013-4792-1, 2014.

501 Ding, Y. H., Wu, P., Liu, Y. J., and Song, Y. F.: Environmental and dynamic conditions for the occurrence of
502 persistent haze events in North China, *Engineering*, 3, 266-271, 10.1016/J.ENG.2017.01.009, 2017.

503 ERA-Interim: PBLH data sets, available at: <http://www.ecmwf.int/en/research/climate-reanalysis/era-interim>, last
504 access: 10 January 2018.

505 Gao, H., and Li, X.: Influences of El Nino Southern Oscillation events on haze frequency in eastern China during
506 boreal winters, *Int J Climatol*, 35, 2682-2688, 10.1002/joc.4133, 2015.

507 Gao, Y., and Chen, D.: A dark October in Beijing 2016, *Atmos Oceanic Sci Lett*, 10, 206-213,
508 10.1080/16742834.2017.1293473, 2017.

509 Guo, J. P., Zhang, X. Y., Wu, Y. R., Zhaxi, Y. Z., Che, H. Z., La, B., Wang, W., and Li, X. W.: Spatio-temporal
510 variation trends of satellite-based aerosol optical depth in China during 1980–2008, *Atmos Environ*, 45,
511 6802-6811, 10.1016/j.atmosenv.2011.03.068, 2011.

512 Guo, S., Hu, M., Zamora, M. L., Peng, J. F., Shang, D. J., Zheng, J., Du, Z. F., Wu, Z. J., Shao, M., Zeng, L. M.,
513 Molina, M. J., and Zhang, R. Y.: Elucidating severe urban haze formation in China, *Proc Natl Acad Sci*, 111,
514 17373-17378, 10.1073/pnas.1419604111, 2014.

515 He, J. H., and Zhu, Z. W.: The relation of South China Sea monsoon onset with the subsequent rainfall over the
516 subtropical East Asia, *Int J Climatol*, 35, 4547-4556, 10.1002/joc.4305, 2015.

517 Held, I. M., and Suarez, M. J.: A proposal for the intercomparison of the dynamical cores of atmospheric general
518 circulation models, *Bull Amer Meteor Soc*, 75, 1825-1830, 10.1175/1520-0477(1994)075<1825:apftio>2.0.co;2,
519 1994.

520 Huang, B. Y., Thorne, P. W., Banzon, V. F., Boyer, T., Chepurin, G., Lawrimore, J. H., Menne, M. J., Smith, T. M.,
521 Vose, R. S., and Zhang, H. M.: Extended Reconstructed Sea Surface Temperature, version 5 (ERSSTv5):
522 Upgrades, validations, and intercomparisons, *J Climate*, 30, 8179-8205, 10.1175/jcli-d-16-0836.1, 2017.

523 [Hurrell, J. W., and Deser, C.: North Atlantic climate variability: The role of the North Atlantic Oscillation, *J*](#)
524 [Marine Syst](#), 78, 28-41, 10.1016/j.jmarsys.2008.11.026, 2009.

525 Jacob, D. J., and Winner, D. A.: Effect of Climate Change on Air Quality, *Atmos Environ*, 43, 51-63,
526 10.1016/j.atmosenv.2008.09.051, 2009.

527 Jia, B., Wang, Y., Yao, Y., and Xie, Y.: A new indicator on the impact of large-scale circulation on wintertime
528 particulate matter pollution over China, *Atmos Chem Phys*, 15, 11919-11929, 10.5194/acp-15-11919-2015,
529 2015.

530 Kalnay, E., Kanamitsu, M., Kistler, R., Collins, W., Deaven, D., Gandin, L., Iredell, M., Saha, S., White, G.,
531 Woollen, J., Zhu, Y., Leetmaa, A., Reynolds, R., Chelliah, M., Ebisuzaki, W., Higgins, W., Janowiak, J., Mo, K.
532 C., Ropelewski, C., Wang, J., Jenne, R., and Joseph, D.: The NCEP/NCAR 40-year reanalysis project, *Bull*
533 *Amer Meteor Soc*, 77, 437-471, 10.1175/1520-0477(1996)077<0437:tnyrp>2.0.co;2, 1996.

534 Lau, K. M., and Kim, K. M.: Observational relationships between aerosol and Asian monsoon rainfall, and
535 circulation, *Geophys Res Lett*, 33, L21810, 10.1029/2006GL027546, 2006.

536 Lau, K. M., Kim, M. K., and Kim, K. M.: Asian summer monsoon anomalies induced by aerosol direct forcing: the
537 role of the Tibetan Plateau, *Clim Dyn*, 26, 855-864, 10.1007/s00382-006-0114-z, 2006.

- 538 Li, C., Martin, R. V., Boys, B. L., van Donkelaar, A., and Ruzzante, S.: Evaluation and application of multi-decadal
539 visibility data for trend analysis of atmospheric haze, *Atmos Chem Phys*, 16, 2435-2457,
540 10.5194/acp-16-2435-2016, 2016.
- 541 Li, Q., Zhang, R. H., and Wang, Y.: Interannual variation of the wintertime fog–haze days across central and
542 eastern China and its relation with East Asian winter monsoon, *Int J Climatol*, 36, 346-354, 10.1002/joc.4350,
543 2016.
- 544 Li, R., Hu, Y. J., Li, L., Fu, H. B., and Chen, J. M.: Real-time aerosol optical properties, morphology and mixing
545 states under clear, haze and fog episodes in the summer of urban Beijing, *Atmos Chem Phys*, 17, 5079-5093,
546 10.5194/acp-17-5079-2017, 2017.
- 547 Li, Z. Q., Lau, W. K. M., Ramanathan, V., Wu, G., Ding, Y., Manoj, M. G., Liu, J., Qian, Y., Li, J., Zhou, T., Fan, J.,
548 Rosenfeld, D., Ming, Y., Wang, Y., Huang, J., Wang, B., Xu, X., Lee, S. S., Cribb, M., Zhang, F., Yang, X., Zhao,
549 C., Takemura, T., Wang, K., Xia, X., Yin, Y., Zhang, H., Guo, J., Zhai, P. M., Sugimoto, N., Babu, S. S., and
550 Brasseur, G. P.: Aerosol and monsoon climate interactions over Asia, *Rev Geophys*, 54, 866-929,
551 10.1002/2015RG000500, 2016.
- 552 Liu, Y., Sun, J. R., and Yang, B.: The effects of black carbon and sulphate aerosols in China regions on East Asia
553 monsoons, *Tellus B*, 61, 642-656, 10.1111/j.1600-0889.2009.00427.x, 2009.
- 554 Luan, T., Guo, X. L., Guo, L. J., and Zhang, T. H.: Quantifying the relationship between PM_{2.5} concentration,
555 visibility and planetary boundary layer height for long-lasting haze and fog–haze mixed events in Beijing,
556 *Atmos Chem Phys*, 18, 203-225, 10.5194/acp-18-203-2018, 2018.
- 557 Mu, M., and Zhang, R. H.: Addressing the issue of fog and haze: A promising perspective from meteorological
558 science and technology, *Sci China Earth Sci*, 57, 1-2, 10.1007/s11430-013-4791-2, 2014.
- 559 Mu, Q., and Liao, H.: Simulation of the interannual variations of aerosols in China: role of variations in
560 meteorological parameters, *Atmos Chem Phys*, 14, 9597-9612, 10.5194/acp-14-9597-2014, 2014.
- 561 NCEP/NCAR: NCEP/NCAR Reanalysis data sets, available at: <http://www.esrl.noaa.gov/psd/data>
562 [/gridded/data.ncep.reanalysis.html](http://www.esrl.noaa.gov/psd/data/gridded/data.ncep.reanalysis.html), last access: 10 January 2018.
- 563 Niu, F., Li, Z. Q., Li, C., Lee, K. H., and Wang, M. Y.: Increase of wintertime fog in China: Potential impacts of
564 weakening of the Eastern Asian monsoon circulation and increasing aerosol loading, *J Geophys Res*, 115,
565 D00K20, 10.1029/2009JD013484, 2010.
- 566 NOAA: NOAA Extended Reconstructed Sea Surface Temperature (SST) V5 data sets, available at:
567 <https://www.esrl.noaa.gov/psd/data/gridded/data.noaa.ersst.v5.html>, last access: 10 January 2018.
- 568 NOAA: NOAA precipitation datasets, available at: <https://www.esrl.noaa.gov/psd/data/gridded/data.prec.html>,
569 last access: 10 January 2018.
- 570 Pei, L., Yan, Z. W., Sun, Z. B., Miao, S. G., and Yao, Y.: Increasing persistent haze in Beijing: potential impacts of
571 weakening East Asian winter monsoons associated with northwestern Pacific sea surface temperature trends,
572 *Atmos Chem Phys*, 18, 3173–3183, 10.5194/acp-18-3173-2018, 2018.
- 573 Pope III, C. A., and Dockery, D. W.: Health effects of fine particulate air pollution: Lines that connect, *J Air Waste*
574 *Manage*, 56, 709-742, 10.1080/10473289.2006.10464485, 2006.
- 575 Seo, J., Kim, J. Y., Youn, D., Lee, J. Y., Kim, H., Lim, Y. B., Kim, Y., and Jin, H. C.: On the multiday haze in the
576 Asian continental outflow: the important role of synoptic conditions combined with regional and local sources,
577 *Atmos Chem Phys*, 17, 9311-9332, 10.5194/acp-17-9311-2017, 2017.

- 578 Takaya, K., and Nakamura, H.: A formulation of a phase-independent wave-activity flux for stationary and
579 migratory quasigeostrophic eddies on a zonally varying basic flow, *J Atmos Sci*, 58, 608-627,
580 10.1175/1520-0469(2001)058<0608:afopi>2.0.co;2, 2001.
- 581 Tao, M. H., Chen, L. F., Xiong, X. Z., Zhang, M. G., Ma, P. F., Tao, J. H., and Wang, Z. F.: Formation process of
582 the widespread extreme haze pollution over northern China in January 2013: Implications for regional air
583 quality and climate, *Atmos Environ*, 98, 417-425, 10.1016/j.atmosenv.2014.09.026, 2014.
- 584 Tao, M. H., Chen, L. F., Wang, Z. F., Wang, J., Tao, J. H., and Wang, X. H.: Did the widespread haze pollution over
585 China increase during the last decade? A satellite view from space, *Environ Res Lett*, 11, 054019,
586 10.1088/1748-9326/11/5/054019, 2016.
- 587 Tett, S. F. B., Stott, P. A., Allen, M. R., Ingram, W. J., and Mitchell, J. F. B.: Causes of twentieth-century
588 temperature change near the Earth's surface, *Nature*, 399, 569-572, 10.1038/21164, 1999
- 589 Tie, X. X., Wu, D., and Brasseur, G.: Lung cancer mortality and exposure to atmospheric aerosol particles
590 in Guangzhou, China, *Atmos Environ*, 43, 2375-2377, 10.1016/j.atmosenv.2009.01.036, 2009.
- 591 Wang, H. J., Chen, H. P., and Liu, J. P.: Arctic sea ice decline intensified haze pollution in eastern China, *Atmos*
592 *Oceanic Sci Lett*, 8, 1-9, 10.3878/AOSL20140081, 2015.
- 593 Wang, H. J., and Chen, H. P.: Understanding the recent trend of haze pollution in eastern China: roles of climate
594 change, *Atmos Chem Phys*, 16, 4205-4211, 10.5194/acp-16-4205-2016, 2016.
- 595 Wang, H. J.: On assessing haze attribution and control measures in China, *Atmos Oceanic Sci Lett*, 11, 120-122,
596 10.1080/16742834.2018.1409067, 2018.
- 597 Wang, J., He, J. H., Liu, X. F., and Wu, B. G.: Interannual variability of the Meiyu onset over Yangtze-Huaihe
598 River Valley and analyses of its previous strong influence signal, *Chin Sci Bull*, 54, 687-695,
599 10.1007/s11434-008-0534-8, 2009.
- 600 Wang, J., Zhang, X. Y., Cai, Z. Y., Wang, D. Z., and Chen, H.: Meteorological causes of a heavy air pollution
601 process in Tianjin and its prediction analyses, *Environ Sci Technol*, 38, 77-82, 2015 (in Chinese).
- 602 Wang, J., Zhao, Q. H., Zhu, Z. W., Qi, L., Wang, J. X. L., and He, J. H.: Interannual variation in the number and
603 severity of autumnal haze days in the Beijing–Tianjin–Hebei region and associated atmospheric circulation
604 anomalies, *Dyn Atmos Oceans*, 84, 1-9, 10.1016/j.dynatmoce.2018.08.001, 2018.
- 605 Wang, Y. S., Yao, L., Wang, L. L., Liu, Z. R., Ji, D. S., Tang, G. Q., Zhang, J. K., Sun, Y., Hu, B., and Xin, J. Y.:
606 Mechanism for the formation of the January 2013 heavy haze pollution episode over central and eastern China,
607 *Sci China Earth Sci*, 57, 14-25, 10.1007/s11430-013-4773-4, 2014.
- 608 Wang, Z. F., Li, J., Wang, Z., Yang, W. Y., Tang, X., Ge, B. Z., Yan, P. Z., Zhu, L. L., Chen, X. S., Chen, H. S.,
609 Wang, W., Li, J. J., Liu, B., Wang, X. Y., Wang, W., Zhao, Y. L., Lu, N., and Su, D. B.: Modeling study of
610 regional severe hazes over mid-eastern China in January 2013 and its implications on pollution prevention and
611 control, *Sci China Earth Sci*, 57, 3-13, 10.1007/s11430-013-4793-0, 2014.
- 612 Wu, D., Tie, X. X., Li, C. C., Ying, Z. M., Kai-Hon Lau, A., Huang, J., Deng, X. J., and Bi, X. Y.: An extremely
613 low visibility event over the Guangzhou region: A case study, *Atmos Environ*, 39, 6568-6577,
614 10.1016/j.atmosenv.2005.07.061, 2005.
- 615 Wu, G. X., Li, Z. Q., Fu, C. B., Zhang, X. Y., Zhang, R. Y., Zhang, R. H., Zhou, T. J., Li, J. P., Li, J. D., Zhou, D.
616 G., Wu, L., Zhou, L. T., He, B., and Huang, R. H.: Advances in studying interactions between aerosols and
617 monsoon in China, *Sci China Earth Sci*, 59, 1-16, 10.1007/s11430-015-5198-z, 2016.

- 618 Xiao, D., Li, Y., Fan, S. J., Zhang, R. H., Sun, J. R., and Wang, Y.: Plausible influence of Atlantic Ocean SST
619 anomalies on winter haze in China, *Theor Appl Climatol*, 122, 249-257, 10.1007/s00704-014-1297-6, 2015.
- 620 Xu, P., Chen, Y. F., and Ye, X. J.: Haze, air pollution, and health in China, *Lancet*, 382, 2067,
621 10.1016/S0140-6736(13)62693-8, 2013.
- 622 Xu, X., Zhao, T., Liu, F., Gong, S. L., Kristovich, D., Lu, C., Guo, Y., Cheng, X., Wang, Y., and Ding, G.: Climate
623 modulation of the Tibetan Plateau on haze in China, *Atmos Chem Phys*, 16, 1365-1375,
624 10.5194/acp-16-1365-2016, 2016.
- 625 Xu, X. D., Wang, Y. J., Zhao, T. L., Cheng, X. H., Meng, Y. Y., and Ding, G. A.: “Harbor” effect of large
626 topography on haze distribution in eastern China and its climate modulation on decadal variations in haze China ,
627 *Chin Sci Bull*, 60, 1132-1143, 10.1360/N972014-00101, 2015 (in Chinese).
- 628 Yang, Y., Liao, H., and Lou, S. J.: Decadal trend and interannual variation of outflow of aerosols from East Asia:
629 Roles of variations in meteorological parameters and emissions, *Atmos Environ*, 100, 141-153,
630 10.1016/j.atmosenv.2014.11.004, 2015.
- 631 Yang, Y., Liao, H., and Lou, S. J.: Increase in winter haze over eastern China in recent decades: Roles of variations
632 in meteorological parameters and anthropogenic emissions, *J Geophys Res Atmos*, 121, 13,050-013,065,
633 10.1002/2016JD025136, 2016.
- 634 Yang, Y. R., Liu, X. G., Qu, Y., An, J. L., Jiang, R., Zhang, Y. H., Sun, Y. L., Wu, Z. J., Zhang, F., Xu, W. Q., and
635 Ma, Q. X.: Characteristics and formation mechanism of continuous hazes in China: a case study during the
636 autumn of 2014 in the North China Plain, *Atmos Chem Phys*, 15, 8165-8178, 10.5194/acp-15-8165-2015, 2015.
- 637 ~~Yin, Z. C., Wang, H. J., and Guo, W. L.: Climatic change features of fog and haze in winter over North China and~~
638 ~~Huang Huai Area, *Sci China Earth Sci*, 58, 1370-1376, 10.1007/s11430-015-5089-3, 2015.~~
- 639 ~~Yin, Z. C., and Wang, H. J.: The relationship between the subtropical Western Pacific SST and haze over~~
640 ~~North-Central North China Plain, *Int J Climatol*, 36, 3479-3491, 10.1002/joc.4570, 2016a.~~
- 641 Yin, Z. C., and Wang, H. J.: Seasonal prediction of winter haze days in the north central North China Plain, *Atmos*
642 *Chem Phys*, 16, 14843-14852, 10.5194/acp-16-14843-2016, 2016b.
- 643 Yin, Z. C., and Wang, H. J.: Role of atmospheric circulations in haze pollution in December 2016, *Atmos Chem*
644 *Phys*, 17, 11673-11681, 10.5194/acp-17-11673-2017, 2017.
- 645 ~~Yin, Z. C., Wang, H. J., and Chen, H. P.: Understanding severe winter haze events in the North China Plain in 2014:~~
646 ~~roles of climate anomalies, *Atmos Chem Phys*, 17, 1641-1651, 10.5194/acp-17-1641-2017, 2017.~~
- 647 ~~Yin, Z. C., and Wang, H. J.: The strengthening relationship between Eurasian snow cover and December haze days~~
648 ~~in central North China after the mid-1990s, *Atmos Chem Phys*, 18, 4753-4763, 10.5194/acp-18-4753-2018,~~
649 ~~2018.~~
- 650 You, T., Wu, R. G., Huang, G., and Fan, G. Z.: Regional meteorological patterns for heavy pollution events in
651 Beijing, *J Meteor Res*, 31, 597-611, 10.1007/s13351-017-6143-1, 2017.
- 652 ~~You, Y. C., Cheng, X. G., Zhao, T. L., Xu, X. D., Gong, S. L., Zhang, X. Y., Zheng, Y., Che, H. Z., Yu, C., Chang, J.~~
653 ~~C., Ma, G. X., and Wu, M.: Variations of haze pollution in China modulated by thermal forcing of the Western~~
654 ~~Pacific Warm Pool, *Atmosphere*, 9, 314, 10.3390/atmos9080314, 2018.~~
- 655 Zhang, H., Zhao, S. Y., Wang, Z. L., Zhang, X. Y., and Song, L. C.: The updated effective radiative forcing of
656 major anthropogenic aerosols and their effects on global climate at present and in the future, *Int J Climatol*, 36,

657 4029-4044, 10.1002/joc.4613, 2016.

658 Zhang, L., Wang, T., Lv, M. Y., and Zhang, Q.: On the severe haze in Beijing during January 2013: Unraveling the
659 effects of meteorological anomalies with WRF-Chem, *Atmos Environ*, 104, 11-21,
660 10.1016/j.atmosenv.2015.01.001, 2015.

661 Zhang, R. H., Li, Q., and Zhang, R. N.: Meteorological conditions for the persistent severe fog and haze event over
662 eastern China in January 2013, *Sci China Earth Sci*, 57, 26-35, 10.1007/s11430-013-4774-3, 2014.

663 Zhang, Z. Y., Zhang, X., Gong, D. Y., Kim, S. J., Mao, R., and Zhao, X.: Possible influence of atmospheric
664 circulations on winter haze pollution in the Beijing–Tianjin–Hebei region, northern China, *Atmos Chem Phys*,
665 16, 561-571, 10.5194/acp-16-561-2016, 2016.

666 Zhao, S. Y., Zhang, H., and Xie, B.: The effects of El Niño–Southern Oscillation on the winter haze pollution of
667 China, *Atmos Chem Phys*, 18, 1863–1877, 10.5194/acp-18-1863-2018, 2018.

668 Zhu, X. W., Tang, G. Q., Hu, B., Wang, L. L., Xin, J. Y., Zhang, J. K., Liu, Z. R., Münkel, C., and Wang, Y. S.:
669 Regional pollution and its formation mechanism over North China Plain: A case study with ceilometer
670 observations and model simulations, *J Geophys Res Atmos*, 121, 14574-14588, 10.1002/2016JD025730, 2016.

671 Zhu, Z. W., Li, T., and He, J. H.: Out-of-Phase relationship between boreal spring and summer decadal rainfall
672 changes in southern China, *J Climate*, 27, 1083-1099, 10.1175/jcli-d-13-00180.1, 2014.

673 Zhu, Z. W., and Li, T.: A new paradigm for continental U.S. summer rainfall variability: Asia–North America
674 teleconnection, *J Climate*, 29, 7313-7327, 10.1175/jcli-d-16-0137.1, 2016.

675 Zhu, Z. W., and Li, T.: The record-breaking hot summer in 2015 over Hawaii and its physical causes, *J Climate*, 30,
676 4253-4266, 10.1175/JCLI-D-16-0438.1, 2017.

677 Zhu, Z. W.: Breakdown of the relationship between Australian summer rainfall and ENSO caused by tropical
678 Indian Ocean SST warming, *J Climate*, 31, 2321-2336, 10.1175/jcli-d-17-0132.1, 2018.

679 Zhu, Z. W., and Li, T.: Amplified contiguous United States summer rainfall variability induced by East Asian
680 monsoon interdecadal change, *Clim Dyn*, 50, 3523-3536, 10.1007/s00382-017-3821-8, 2018.

681 Zou, Y. F., Wang, Y. H., Zhang, Y. Z., and Koo, J.-H.: Arctic sea ice, Eurasia snow, and extreme winter haze in
682 China, *Sci Adv*, 3, e1602751, 10.1126/sciadv.1602751, 2017.

683 [Zuo, J. Q., Li, W. J., Sun, C. H., Xu, L., and Ren, H. L.: Impact of the North Atlantic sea surface temperature](#)
684 [tripole on the East Asian summer monsoon, *Adv Atmos Sci*, 30, 1173-1186, 10.1007/s00376-012-2125-5, 2013.](#)
685
686
687
688
689
690
691
692
693
694
695
696

697 Figures Captions

698 **Figure 1.** Topographic map (shaded; m) for the BTH region and the locations of 20 meteorological sites (colored dots). The dots colored
699 red (light red; magenta) represent significant positive temporal correlation coefficients at the 99% (95%; 90%) confidence level between
700 the AHD_{BTH} and AHD for every individual site on the interannual timescale.

701 **Figure 2.** Time series of the raw AHD_{BTH} (black line; days), along with its interdecadal component (blue line; days) and interannual
702 component (red line; days), for the period 1960–2017. The gray horizontal line delineates the average climate value of the raw AHD_{BTH}
703 during 1960–2017.

704 **Figure 3.** The climatological-mean (1960–2017) autumnal (a) Z500 (contours; gpm), UV850 (vectors; $m s^{-1}$) and total cloud (shaded; %),
705 and (b) surface relative humidity (shaded; %) and surface air temperature (contours; $^{\circ}C$). The gray shaded area denotes the Tibetan
706 Plateau, and the blue dashed box delineates the research domain of the BTH region. The letter A represents the center of anticyclonic
707 circulation.

708 **Figure 4.** Regressed patterns of autumnal meteorological parameters onto the interannual component of the AHD_{BTH} , including (a)
709 surface relative humidity (shaded; %), (b) surface air temperature (shaded; $^{\circ}C$), (c) surface wind speed (shaded; $m s^{-1}$), (d) SLP (shaded;
710 hPa), (e) PBLH (shaded; m), and (f) 500-hPa omega (shaded; $10^{-2} Pa s^{-1}$). Regression coefficients that are significant at the 90%
711 confidence level are stippled. The blue dashed box outlines the research domain of the BTH region.

712 **Figure 5.** Regressed anomalies of autumnal (a) 200-hPa geopotential height (Z200; shaded; gpm) and 200-hPa winds (UV200; vectors; m
713 s^{-1}), (b) Z500 (shaded; gpm) and 500-hPa winds (UV500; vectors; $m s^{-1}$), (c) SST (shaded; $^{\circ}C$) and UV850 (vectors; $m s^{-1}$), (d) SLP
714 (shaded; hPa) and surface winds (vectors; $m s^{-1}$), and (e) precipitation (shaded; $mm day^{-1}$), with respect to the interannual component of
715 the AHD_{BTH} . Regression coefficients that are significant at the 95% (90%) confidence level are stippled (cross hatched). In panels (a) and
716 (b), only the wind vectors with statistical significance above the 90% confidence level are shown. In panel (c), the two red dashed
717 rectangles, labelled R1 and R2, are the key regions where SSTAs are significantly correlated with the interannual component of the
718 AHD_{BTH} ; vectors with scales less than $0.05 m s^{-1}$ are omitted. In panel (d), vectors with scales less than $0.03 m s^{-1}$ are omitted. The blue
719 dashed box delineates the research domain of the BTH region. The letters A and C represent the centers of anticyclonic and cyclonic
720 anomalies, respectively.

721 **Figure 6.** Time series of the normalized interannual component of the AHD_{BTH} (black line), along with the simultaneous SST over R1
722 (red line) and R2 (blue line) for the period 1960–2017. The horizontal dashed lines denote 0.8 of the standard deviation. The numerals
723 labelled at the bottom represent the correlation coefficients (r) between the AHD_{BTH} and simultaneous SST over R1 and R2, separately.
724 The upper and lower dots in the red line indicate the three highest and lowest years of SST over R1, respectively.

725 **Figure 7.** Regressed anomalies of autumnal UV850 (vectors; $m s^{-1}$) with respect to the simultaneous interannual component of the SST
726 over R1. Green arrows represent the wind vectors with statistical significance above the 90% confidence level. The red dashed rectangle
727 labelled R1 is the key region where SSTAs are significantly correlated with the interannual component of the AHD_{BTH} . The blue dashed
728 box delineates the research domain of the BTH region. The gray shaded area denotes the Tibetan Plateau. The letters A and C represent
729 the centers of anticyclonic and cyclonic anomalies, respectively.

730 **Figure 8.** The autumnal composite differences of (a) 200-hPa and (b) 500-hPa WAF (vectors; $m^2 s^{-2}$), geopotential height (contours;
731 gpm), and relative vorticity (shaded; $10^{-5} s^{-1}$) between the three highest and three lowest years of simultaneous SST over R1 (highest
732 minus lowest), as shown in Fig. 6. The red dashed rectangle labelled R1 is the key region where SSTAs are significantly correlated with
733 the interannual component of the AHD_{BTH} . The blue dashed box delineates the research domain of the BTH region.

734 **Figure 9.** Regressed anomalies of autumnal (a) UV850 (vectors; $m s^{-1}$) and SST (shaded; $^{\circ}C$), and (b) precipitation (shaded; $mm day^{-1}$)
735 with respect to the simultaneous interannual component of the SST over R2. In panel (a), green arrows represent the wind vectors with
736 statistical significance above the 99% confidence level, and vectors with scales less than $0.05 m s^{-1}$ are omitted. Regression coefficients
737 that are significant at the 99% confidence level are cross hatched. The dashed red rectangle labelled R2 is the key region where SSTAs are
738 significantly correlated with the interannual component of the AHD_{BTH} . The blue dashed box delineates the research domain of the BTH
739 region. The gray shaded area denotes the Tibetan Plateau. The letter A (C) represents the center of anticyclonic (cyclonic) anomaly.

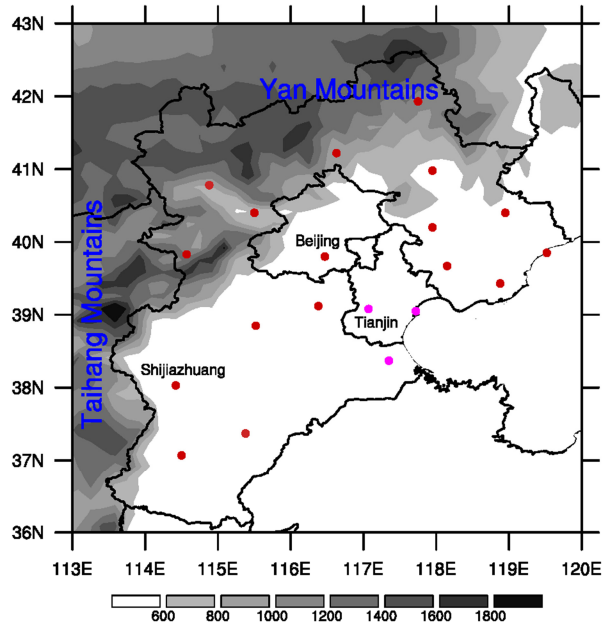
740 **Figure 10.** (a) Latitude–vertical section (112.5° – $130^{\circ}E$) of the autumnal omega (shaded; $10^{-2} Pa s^{-1}$) and (b) longitude–vertical section
741 (35° – $42.5^{\circ}N$) of the autumnal air temperature (shaded; $^{\circ}C$) anomalies regressed onto the simultaneous interannual component of the SST
742 over R2. Regression coefficients that are significant at the 90% confidence level are stippled. The thick blue horizontal bars superimposed
743 onto the abscissa of panels (a) and (b) indicate the latitudes and longitudes of the BTH region, respectively.

744 **Figure 11.** The response of anomalous (a) Z200 (shaded; 10 gpm) and UV200 (vectors; $m s^{-1}$), and (b) Z500 (shaded; 10 gpm) and
745 UV500 (vectors; $m s^{-1}$) in H_NAS . The red contours indicate the imposed idealized heating. The blue dashed box delineates the research
746 domain of the BTH region. The letters A and C represent the centers of anticyclonic and cyclonic anomalies, respectively.

747 **Figure 12.** The response of Z850 (shaded; 10 gpm) and UV850 (vectors; $m s^{-1}$) in H_WNP . The magenta contours indicate the imposed
748 idealized heating. The blue dashed box delineates the research domain of the BTH region. The gray shaded area denotes the Tibetan
749 Plateau. The letter A (C) represents the center of anticyclonic (cyclonic) anomaly.

750 **Figure 13.** Schematic diagram encapsulating the SSTA-induced (warming in R1 and R2) physical mechanisms and pathways connected
751 to above-normal AHD_{BTH} years on the interannual timescale. Anomalous quasi-barotropic anticyclones (A) and cyclones (C) are indicated
752 by blue and red elliptical cycles with arrows separately, denoting large-scale Rossby wave train triggered by the heating to the north of R1.
753 Green arrows depict the key horizontal low-level (850-hPa) airflows. The red, azure and green arrows together exhibit the vertical
754 overturning circulation tied to the SST warming in R2. The left-hand (right-hand) side of the cloud-resembled pattern with violet short
755 dashed lines presents the significant anomalous precipitation induced by SSTAs over R1 (R2). The blue dashed box delineates the
756 research domain of the BTH region.

757



758

759 **Figure 1.** Topographic map (shaded; m) for the BTH region and the locations of 20 meteorological sites (colored dots). The dots colored
 760 red (light red; magenta) represent significant positive temporal correlation coefficients at the 99% (95%; 90%) confidence level between
 761 the AHD_{BTH} and AHD for every individual site on the interannual timescale.

762

763

764

765

766

767

768

769

770

771

772

773

774

775

776

777

778

779

780

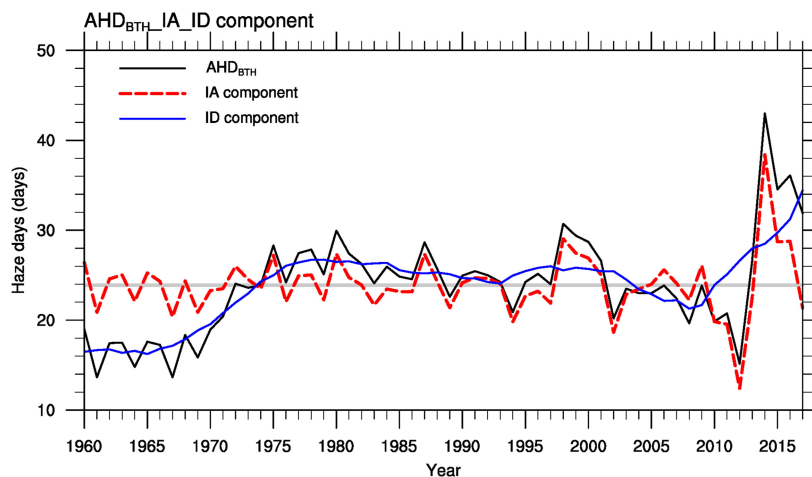
781

782

783

784

785



786

787 **Figure 2.** Time series of the raw AHD_{BTH} (black line; days), along with its interdecadal component (blue line; days) and interannual
 788 component (red line; days), for the period 1960–2017. The gray horizontal line delineates the average climate value of the raw AHD_{BTH}
 789 during 1960–2017.

790

791

792

793

794

795

796

797

798

799

800

801

802

803

804

805

806

807

808

809

810

811

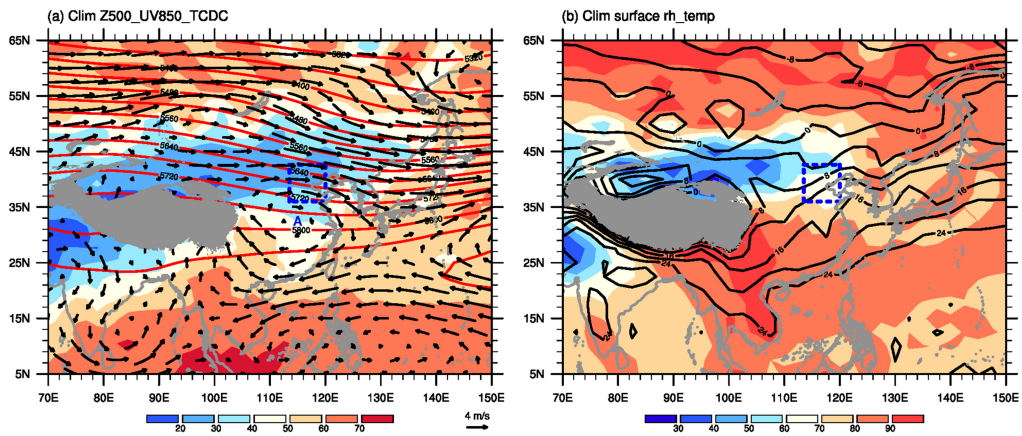
812

813

814

815

816



817

818 **Figure 3.** The climatological-mean (1960–2017) autumnal (a) Z500 (contours; gpm), UV850 (vectors; m s^{-1}) and total cloud (shaded; %),
 819 and (b) surface relative humidity (shaded; %) and surface air temperature (contours; $^{\circ}\text{C}$). The gray shaded area denotes the Tibetan
 820 Plateau, and the blue dashed box delineates the research domain of the BTH region. The letter A represents the center of anticyclonic
 821 circulation.

822

823

824

825

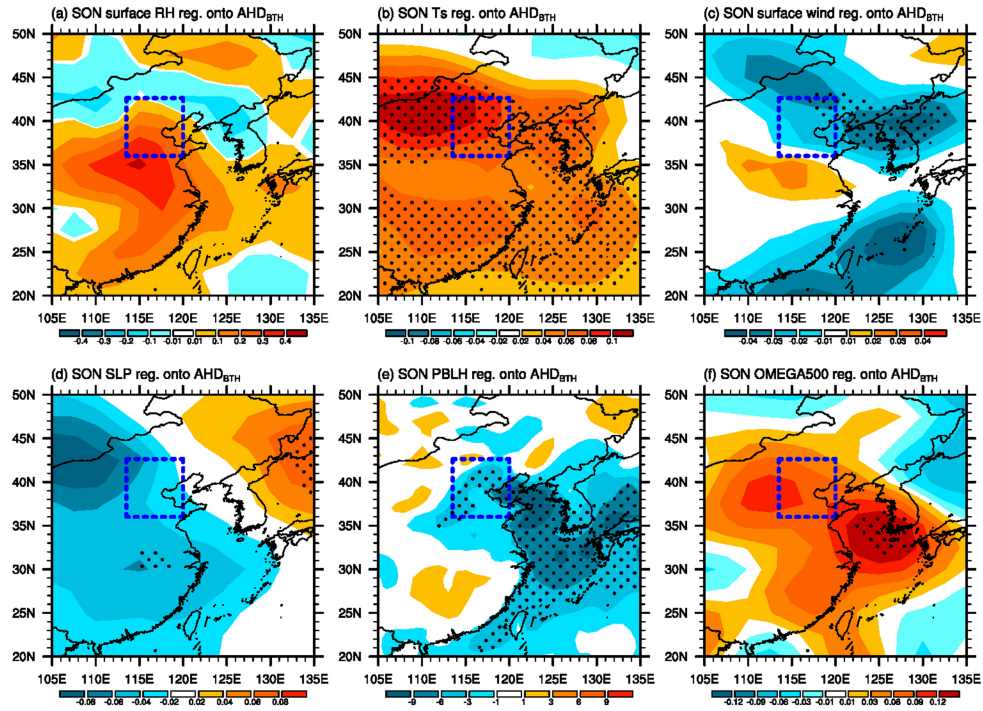
826

827

828

829

830



831

832 **Figure 4.** Regressed patterns of autumnal meteorological parameters onto the interannual component of the AHD_{BTH} , including (a)
 833 surface relative humidity (shaded; %), (b) surface air temperature (shaded; $^{\circ}C$), (c) surface wind speed (shaded; $m s^{-1}$), (d) SLP (shaded;
 834 hPa), (e) PBLH (shaded; m), and (f) 500-hPa omega (shaded; $10^{-2} Pa s^{-1}$). Regression coefficients that are significant at the 90%
 835 confidence level are stippled. The blue dashed box outlines the research domain of the BTH region.

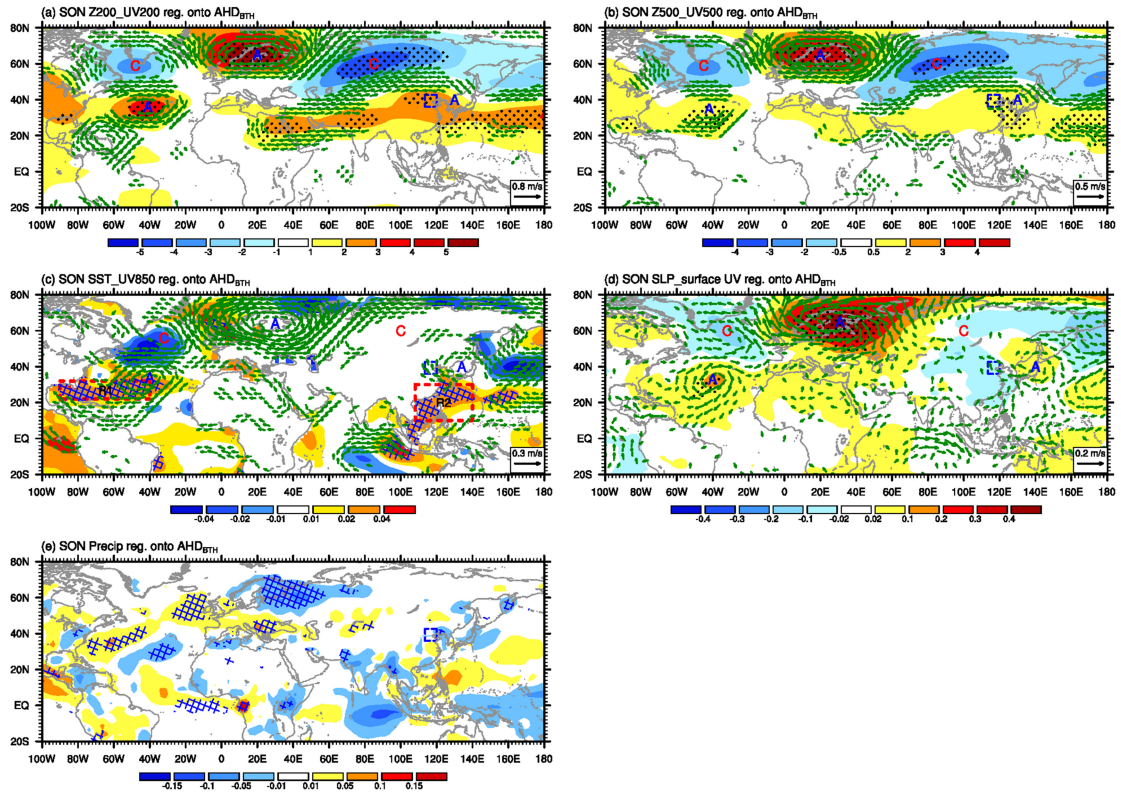
836

837

838

839

840



841

842 **Figure 5.** Regressed anomalies of autumnal (a) 200-hPa geopotential height (Z200; shaded; gpm) and 200-hPa winds (UV200; vectors; m s^{-1}), (b) Z500 (shaded; gpm) and 500-hPa winds (UV500; vectors; m s^{-1}), (c) SST (shaded; $^{\circ}\text{C}$) and UV850 (vectors; m s^{-1}), (d) SLP (shaded; hPa) and surface winds (vectors; m s^{-1}), and (e) precipitation (shaded; mm day^{-1}), with respect to the interannual component of the AHD_{BTH} . Regression coefficients that are significant at the 95% confidence level are stippled (cross hatched). In panels (a) and (b), only the wind vectors with statistical significance above the 90% confidence level are shown. In panel (c), the two red dashed rectangles, labelled R1 and R2, are the key regions where SSTAs are significantly correlated with the interannual component of the AHD_{BTH} ; vectors with scales less than 0.05 m s^{-1} are omitted. In panel (d), vectors with scales less than 0.03 m s^{-1} are omitted. The blue dashed box delineates the research domain of the BTH region. The letters A and C represent the centers of anticyclonic and cyclonic anomalies, respectively.

851

852

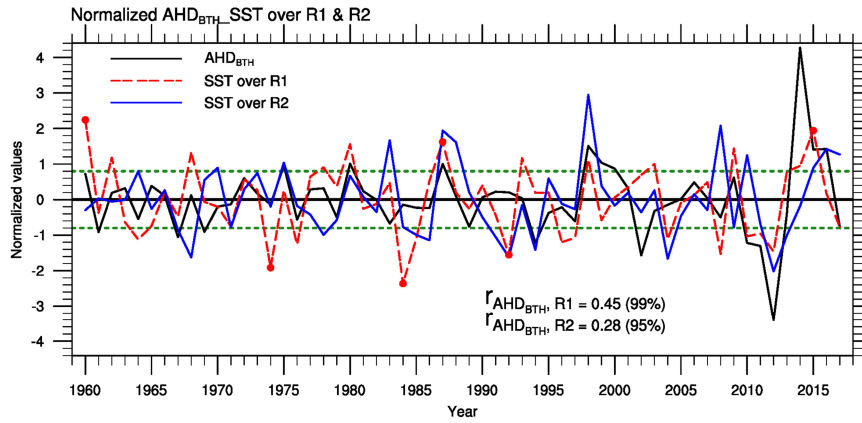
853

854

855

856

857



858

859 **Figure 6.** Time series of the normalized interannual component of the AHD_{BTH} (black line), along with the simultaneous SST over R1
 860 (red line) and R2 (blue line) for the period 1960–2017. The horizontal dashed lines denote 0.8 of the standard deviation. The numerals
 861 labelled at the bottom represent the correlation coefficients (*r*) between the AHD_{BTH} and simultaneous SST over R1 and R2, separately.
 862 The upper and lower dots in the red line indicate the three highest and lowest years of SST over R1, respectively.

863

864

865

866

867

868

869

870

871

872

873

874

875

876

877

878

879

880

881

882

883

884

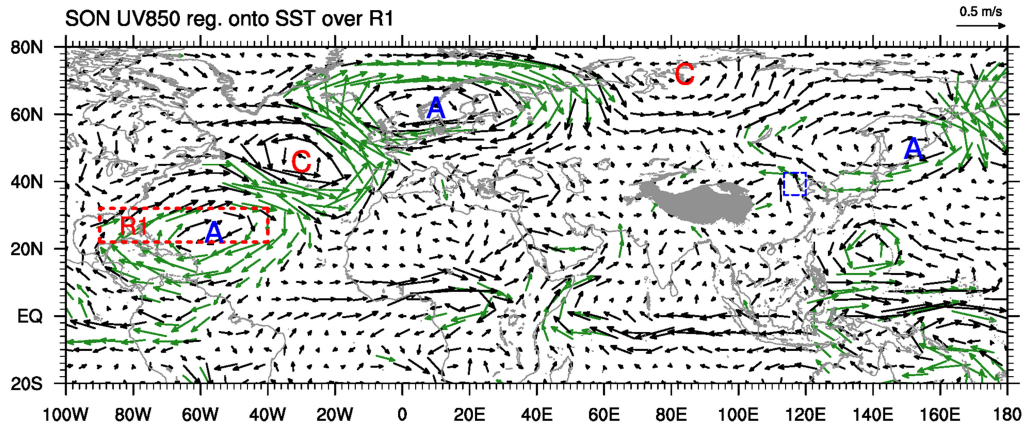
885

886

887

888

889



890

891 **Figure 7.** Regressed anomalies of autumnal UV850 (vectors; m s^{-1}) with respect to the simultaneous interannual component of the SST
 892 over R1. Green arrows represent the wind vectors with statistical significance above the 90% confidence level. The red dashed rectangle
 893 labelled R1 is the key region where SSTAs are significantly correlated with the interannual component of the AHD_{BTH} . The blue dashed
 894 box delineates the research domain of the BTH region. The gray shaded area denotes the Tibetan Plateau. The letters A and C represent
 895 the centers of anticyclonic and cyclonic anomalies, respectively.

896

897

898

899

900

901

902

903

904

905

906

907

908

909

910

911

912

913

914

915

916

917

918

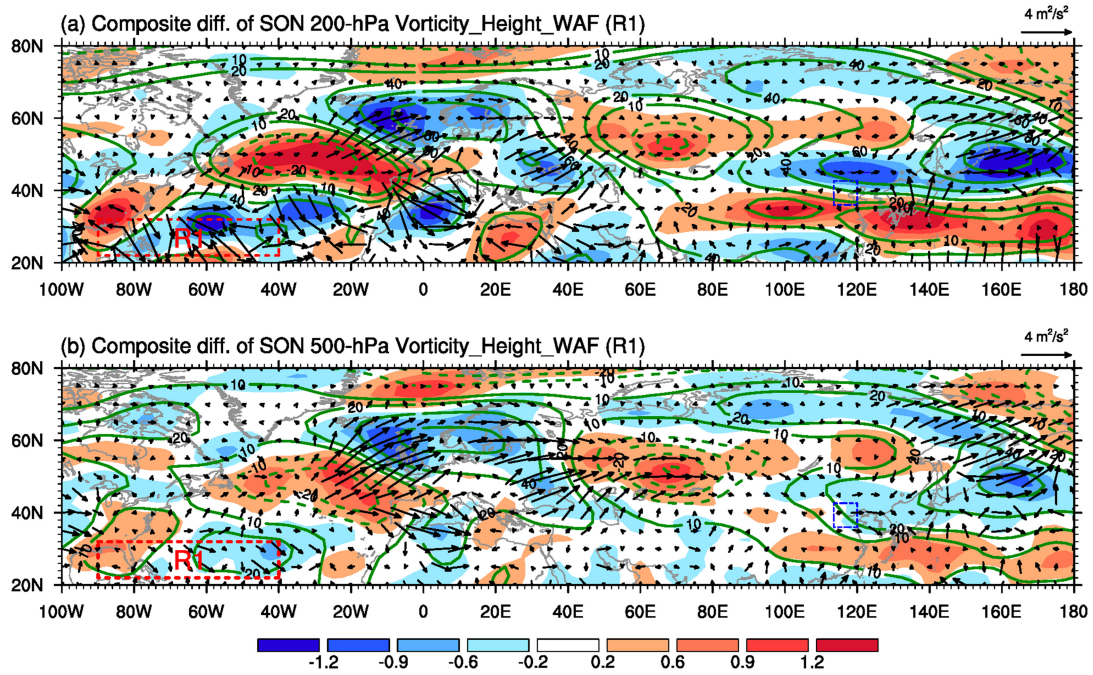
919

920

921

922

923



924

925 **Figure 8.** The autumnal composite differences of (a) 200-hPa and (b) 500-hPa WAF (vectors; $m^2 s^{-2}$), geopotential height (contours;
 926 gpm), and relative vorticity (shaded; $10^{-5} s^{-1}$) between the three highest and three lowest years of simultaneous SST over R1 (highest
 927 minus lowest), as shown in Fig. 6. The red dashed rectangle labeled R1 is the key region where SSTAs are significantly correlated with
 928 the interannual component of the AHD_{BTH} . The blue dashed box delineates the research domain of the BTH region.

929

930

931

932

933

934

935

936

937

938

939

940

941

942

943

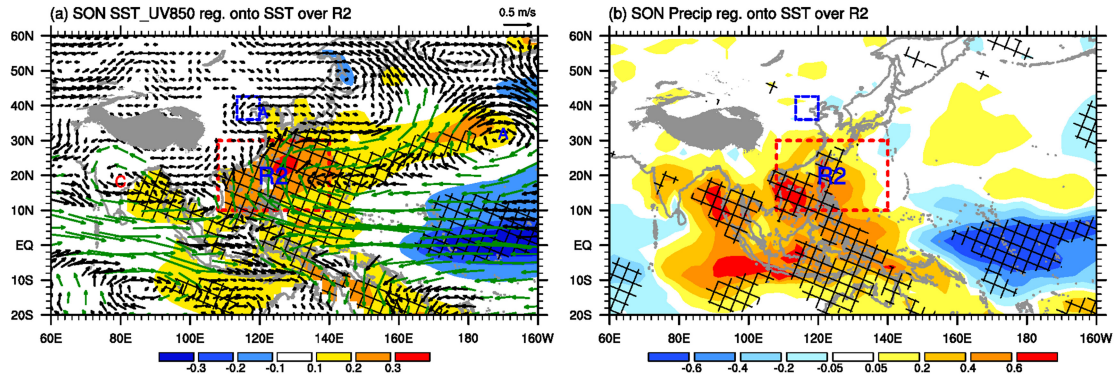
944

945

946

947

948



949

950 **Figure 9.** Regressed anomalies of autumnal **(a)** UV850 (vectors; m s^{-1}) and SST (shaded; $^{\circ}\text{C}$), and **(b)** precipitation (shaded; mm day^{-1})
 951 with respect to the simultaneous interannual component of the SST over R2. In panel **(a)**, green arrows represent the wind vectors with
 952 statistical significance above the 99% confidence level, and vectors with scales less than 0.05 m s^{-1} are omitted. Regression coefficients
 953 that are significant at the 99% confidence level are cross hatched. The dashed red rectangle labelled R2 is the key region where SSTAs are
 954 significantly correlated with the interannual component of the AHD_{BTH} . The blue dashed box delineates the research domain of the BTH
 955 region. The gray shaded area denotes the Tibetan Plateau. The letter A (C) represents the center of anticyclonic (cyclonic) anomaly.

956

957

958

959

960

961

962

963

964

965

966

967

968

969

970

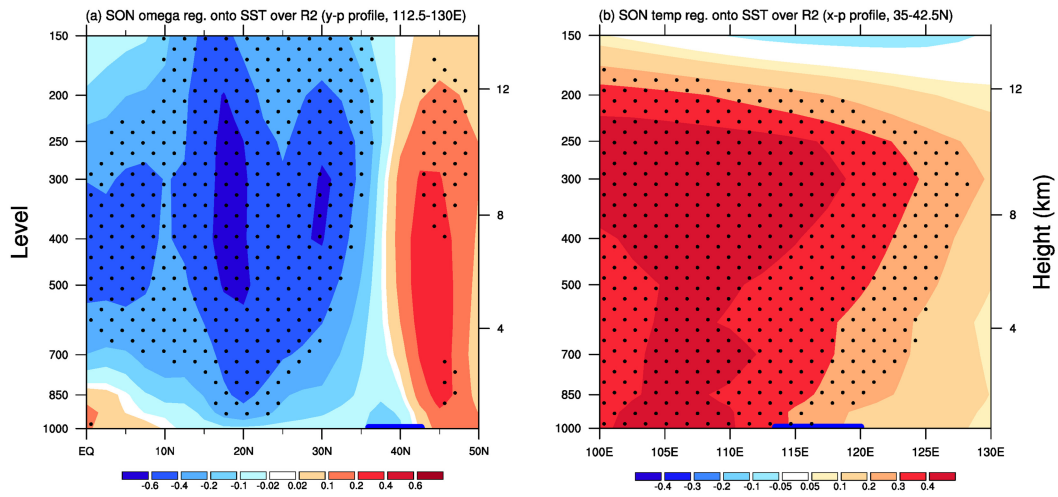
971

972

973

974

975



976

977 **Figure 10.** (a) Latitude-vertical section (112.5°–130°E) of the autumnal omega (shaded; $10^{-2} \text{ Pa s}^{-1}$) and (b) longitude-vertical section
 978 (35°–42.5°N) of the autumnal air temperature (shaded; °C) anomalies regressed onto the simultaneous interannual component of the SST
 979 over R2. Regression coefficients that are significant at the 90% confidence level are stippled. The thick blue horizontal bars superimposed
 980 onto the abscissa of panels (a) and (b) indicate the latitudes and longitudes of the BTH region, respectively.

981

982

983

984

985

986

987

988

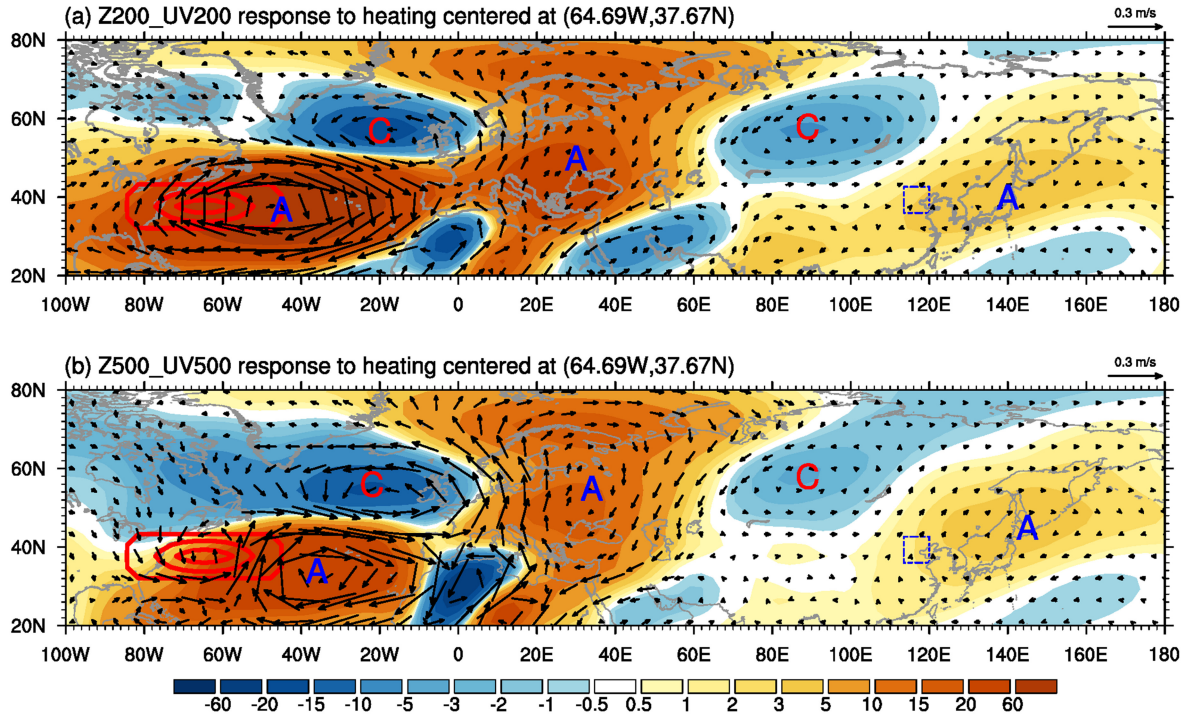
989

990

991

992

993



994

995 **Figure 11.** The response of anomalous (a) Z200 (shaded; 10 gpm) and UV200 (vectors; $m s^{-1}$), and
 996 (b) Z500 (shaded; 10 gpm) and UV500 (vectors; $m s^{-1}$) in H_NAS. The red contours indicate the imposed idealized heating. The blue dashed box delineates the research
 997 domain of the BTH region. The letters A and C represent the centers of anticyclonic and cyclonic anomalies, respectively.

998

999

1000

1001

1002

1003

1004

1005

1006

1007

1008

1009

1010

1011

1012

1013

1014

1015

1016

1017

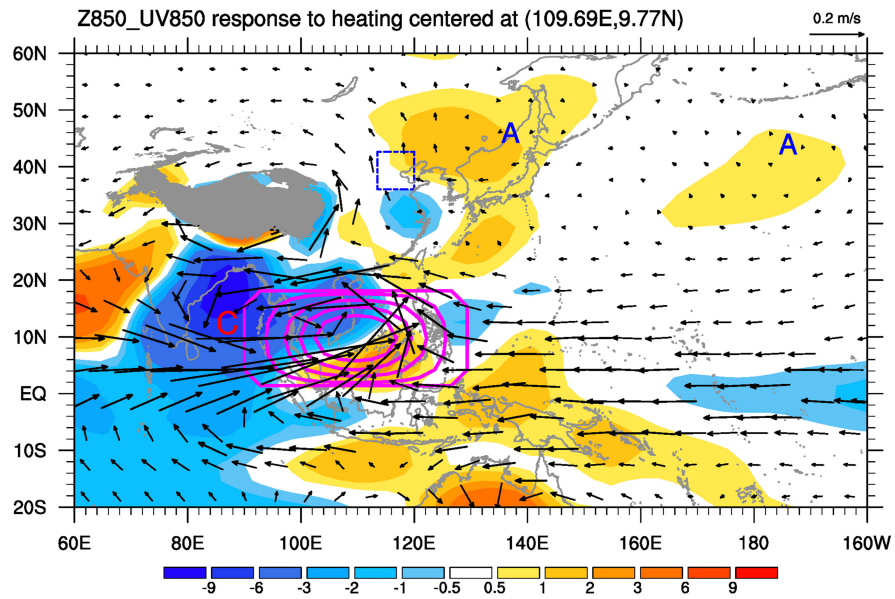
1018

1019

1020

1021

1022



1023

1024 **Figure 12.** The response of Z850 (shaded; 10 gpm) and UV850 (vectors; m s^{-1}) in H_WNP. The magenta contours indicate the imposed
1025 idealized heating. The blue dashed box delineates the research domain of the BTH region. The gray shaded area denotes the Tibetan
1026 Plateau. The letter A (C) represents the center of anticyclonic (cyclonic) anomaly.

1027

1028

1029

1030

1031

1032

1033

1034

1035

1036

1037

1038

1039

1040

1041

1042

1043

1044

1045

1046

1047

1048

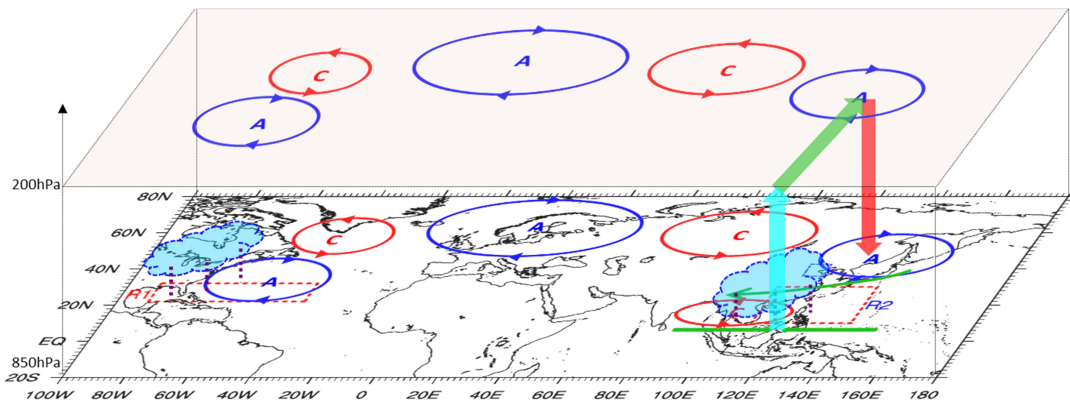
1049

1050

1051

1052

1053



1054

1055 **Figure 13.** Schematic diagram encapsulating the SSTA-induced (warming in R1 and R2) physical mechanisms and pathways connected to above-normal AHD_{BTH} years on the interannual timescale. Anomalous quasi-barotropic anticyclones (A) and cyclones (C) are indicated by blue and red elliptical cycles with arrows separately, denoting large-scale Rossby wave train triggered by the heating to the north of R1. Green arrows depict the key horizontal low-level (850-hPa) airflows. The red, azure and green arrows together exhibit the vertical overturning circulation tied to the SST warming in R2. The left-hand (right-hand) side of the cloud-resembled pattern with violet short dashed lines presents the significant anomalous precipitation induced by SSTAs over R1 (R2). The blue dashed box delineates the research domain of the BTH region.

1062

1063

1064

1065

1066

1067

1068

1069

1070

1071

1072

1073

1074

1075

1076

1077

1078

1079

1080

1081

1082

1083

1084

1085

1086

1087

1088